

## REVIEW ARTICLE OPEN



# Interface enhanced functionalities in oxide superlattices under mechanical and electric boundary conditions

Hongwei Wang<sup>1</sup>, Fujie Tang<sup>1</sup>, Pratikumar H. Dhuvad<sup>1</sup> and Xifan Wu<sup>1,2</sup>✉

In recent years, the inverse design of artificial materials, in the format of thin-films and superlattices, has been an active sub-field in material science. From a joint effort from both experiment and theory, scientists are searching for new engineering methods or design rules so that the materials can be custom designed with desired functionalities in theory before the materials are actually synthesized by epitaxial growth technique in laboratory. In this article, we provide a short summary of the recently proposed epitaxial strain and interface design approaches for the functional artificial oxide heterostructures. The underlying physical mechanism enabling the enhanced functional properties, such as ferroelectricity and multiferroics, are briefly reviewed. In particular, focused discussions are made on the proper treatments of both mechanical and electric boundary conditions when the oxide thin-films and superlattices are theoretically modeled by first-principles computer simulations.

*npj Computational Materials* (2020)6:52; <https://doi.org/10.1038/s41524-020-0326-5>

## INTRODUCTION

Last few decades have witnessed the explosive growth of new materials<sup>1–8</sup>. A large portion of recently synthesized materials are contributed by the so-called artificial materials which cannot naturally exist. Such a significant progress has been facilitated by the advent and the maturity of modern thin-film technology<sup>9</sup>, for example, the pulsed laser deposition<sup>10</sup> and the molecular beam epitaxy<sup>11</sup>. Based on these advanced epitaxial techniques, it has become a routine work to make oxide superlattices or heterostructures in the laboratories. In particular, in these quasi one-dimensional materials of superlattices, sharp interfaces are formed which are defined by the atomic-level flat surface terraces bringing two distinct parent oxides into one artificial material<sup>8</sup>.

Equipped with the advanced synthesis techniques, scientists are now focusing on searching for materials with target properties. In practice, the functional properties include large ferroelectric (FE)<sup>12</sup> and ferromagnetic (FM) moments, piezoelectric<sup>12</sup>, elastic, dielectric responses<sup>13</sup>, magnetoelastic, and spin-structural couplings<sup>7,14–17</sup>, as well as tunable optical bandgap<sup>18</sup>. Very often, multifunctional properties are desired to be possessed in a single material for device applications. However, it implies an inverse design of materials, which poses a major challenge by itself. The difficulty lies at the fact that one need to search within the greatly expanded class of artificial materials. In oxide superlattice, one unique interface is formed by any two parent oxides. While, once the superlattices at the nanoscale are concerned, the complexity rapidly grows when one is facing almost infinite ways to select the particular interfaces and later, to arrange them into the superlattices<sup>19</sup>. The situation is even worse when one is provided by many choices of substrates in coherent growths of the heterostructures.

Clearly, efficient design principles are critically needed in order to guide the experimental exploration before the superlattice are actually grown in laboratory. In the past years, important inverse design principles have been proposed in theory<sup>13,17,20</sup> and later been verified in experiments<sup>1,7,21–23</sup>. On the one hand, the motif of interface introduces an extra tuning knob to modify the

symmetry of the heterostructures. The interfaces can naturally break the compositional inversion symmetry and generate the self-poling effects in the superlattice, which are used to induce or enhance the FE polarization and dielectric responses<sup>24</sup>. On the other hand, the interface itself plays a key role to determine the functionalities of the superlattice. Different physical properties of bulk oxides strongly interact with each other, and the interface is at the forefront of the battle field where the reconstructions can lead to nontrivial physical effects. In the sparse interface limit, the interfaces are spread out and the overall properties of the superlattice are mainly governed by the long-range electrostatic interactions mediated by interfaces which is known as the electrostatic coupling effect and has been widely applied<sup>24,25</sup>. However, in the dense interface limit, the short-range interactions will be decisive. The inversion symmetry can break right at the interface by two different types of structural distortions<sup>26–28</sup>. Moreover, large electronic and structural reconstructions can occur at the interfaces. In some cases, the interfacial reconstructions can be utilized to stabilize some highly functional phases that are metastable in bulk materials<sup>8</sup>.

Ab initio calculations are actively involved throughout the arrival of interface design mechanism. Based on density functional theory (DFT)<sup>29</sup>, first-principles calculations not only allow the initial quick validation of conceived design methods, but also give important qualitative or even quantitative inputs for future experiments. DFT can be dated back to 1960s, the theory rigorously projects the formidable many interacting electrons in condensed matter system onto an equivalent noninteracting one electron system. The successful application of DFT relies on the adopted level of exchange correlation (XC) functional approximations, which effectively describes the many-body effect of electrons. While the local density approximation (LDA)<sup>30,31</sup> underestimates the structural distortion, the generalized gradient approximation (GGA)<sup>32</sup> suffers from the so-called super-tetragonality error and often overestimates the structure distortions<sup>33</sup>. By satisfying all seventeen known exact constraints on semi-local XC functionals, the recently developed strongly constrained and

<sup>1</sup>Department of Physics, Temple University, Philadelphia, PA 19122, USA. <sup>2</sup>Institute for Computational Molecular Science, Temple University, Philadelphia, PA 19122, USA. ✉email: [xifanwu@temple.edu](mailto:xifanwu@temple.edu)

appropriately normed (SCAN) meta-GGA functional<sup>34,35</sup> improves over the traditional LDA/GGA for structural, electric, and energetic properties of diversely bonded FE and multiferroic materials. The more expensive ab initio calculation based on the random phase approximation (RPA) has been only occasionally applied to study perovskite<sup>36</sup>. The capability of DFT to describe functional materials has been greatly enhanced along with the development of electronic structure theory, such as modern theory of polarization, density functional perturbation theory (DFPT)<sup>37–40</sup>, etc. The functionalities including intrinsic properties such as FE and FM moment which can be computed by standard DFT, or responses to various stimuli such as piezoelectric and dielectric constants calculable by DFPT.

While modeling the oxide superlattices, extra care should be taken on the mechanical and the electric boundary conditions. The mechanical boundary condition mainly refers to the epitaxial strain applied by the substrates. In the superlattice, the lattice constant of the substrate is usually different from that of bulk oxides<sup>41</sup>. As a result, either a compressive or a tensile strain is applied. The applied strain can be strongly coupled to the polar phonon mode<sup>15,42,43</sup> or the magnetic exchange interaction. Such couplings have been applied to engineer functional properties such as FE and FM in multiferroics<sup>7,15,17</sup>. As far as the electric boundary condition is concerned, either a fixed electric ( $\mathbf{E}$ ) field or a fixed electric displacement ( $\mathbf{D}$ ) field is applied, which correspond to the close-circuit or the open-circuit condition in device applications<sup>19,44–46</sup>. Furthermore, the correct treatment of electric boundary condition is also the key to describe the localized interface effect in insulating oxide superlattice. Such interface information can be extracted and used later to construct new superlattice for an inverse design purpose. In the above, throughout the superlattice, the  $\mathbf{D}$ -field instead of  $\mathbf{E}$ -field should be the uniform parameter due to charge continuity principle.

In this article, we firstly review the theoretical techniques in modeling the oxide thin-films and superlattices in section of “First-principles modeling and computational methods”, in which the recent methodology development enabling the calculations of insulating nonlinear materials under applied electric field and applied electric displacement field are reviewed. In the section of “Induced or enhanced functional properties under epitaxial strain”, we briefly describe the enhanced functionalities discovered by mismatch strains and the underlying physics. In the section of “Interface induced functional FE and multiferroic properties”, we review the four recently proposed interface design mechanism, which are the inversion symmetry breaking in tricolor superlattice in the section of “Compositional inversion symmetry breaking”, the electrostatic coupling mechanism in the section of

“Electrostatic coupling effect via interfaces”, hybrid improper ferroelectricity in oxide heterostructure in the section of “Hybrid improper ferroelectricity”, and interface stabilized BiFeO<sub>3</sub>-like structures in the section of “Interfacial reconstructions of structural instabilities”. The physical principles behind each of the above design rules are explained in detail.

## FIRST-PRINCIPLES MODELING AND COMPUTATIONAL METHODS

### Mechanical boundary condition: epitaxial strain

Functional properties of oxide superlattices, such as FM<sup>47,48</sup>, superconductivity<sup>49,50</sup>, tunable optical band gap<sup>18,51</sup>, FE<sup>9,41,52,53</sup>, piezoelectricity<sup>9,54,55</sup>, and multiferroicity<sup>56–59</sup>, can be effectively optimized or even induced by the mechanical boundary conditions via the mismatch between bulk materials and the substrates on which the thin-films are grown. In general, the epitaxial strain  $\eta$  is defined as  $\eta = (a - a_0)/a_0$ , where  $a$  and  $a_0$  are the in-plane lattice constants of the substrate and the bulk materials to be strained, respectively. More subtly, the epitaxial strains can be further categorized as homogeneous or anisotropic bi-axial strain<sup>60</sup> if the two in-plane lattice constants are strained by same or different amounts, respectively. Over the last 2 decades, a vast number of perovskites have been successfully utilized as substrates in the synthesis of artificial thin-films<sup>41,61–64</sup>. With such a broad range of lattice constants as shown in Fig. 1, the mismatch strain can be experimentally adjusted within [−3%, 3%] for many perovskites<sup>64</sup>. However, in DFT calculations, the atomic modeling of such strained thin-films is rather straightforward, unlike the cases in the experiment. In order to mimic the coherent thin-film growth, the first-principles calculations should be performed by minimizing the total energy with the in-plane lattice constants clamped to be the same as the selected substrates, while all the other degrees of freedom including force on each atom as well as the stress along the growth direction should be fully relaxed. For materials with magnetic ordering, the modeling is slightly more complicated since the proper supercell size should be chosen in such a way that the particular type of antiferromagnetic (AFM) ordering<sup>65,66</sup> or the noncollinear spin configuration<sup>67,68</sup> are properly accommodated. However, it should be kept in mind that the coherent growth can be only achieved with the thickness below 10–20 nm<sup>46</sup>. If it is above critical thickness, the strain energy would be relaxed to their natural bulk values<sup>60,64</sup>, sometimes accompanied by the development of threading dislocations<sup>46,64</sup>.

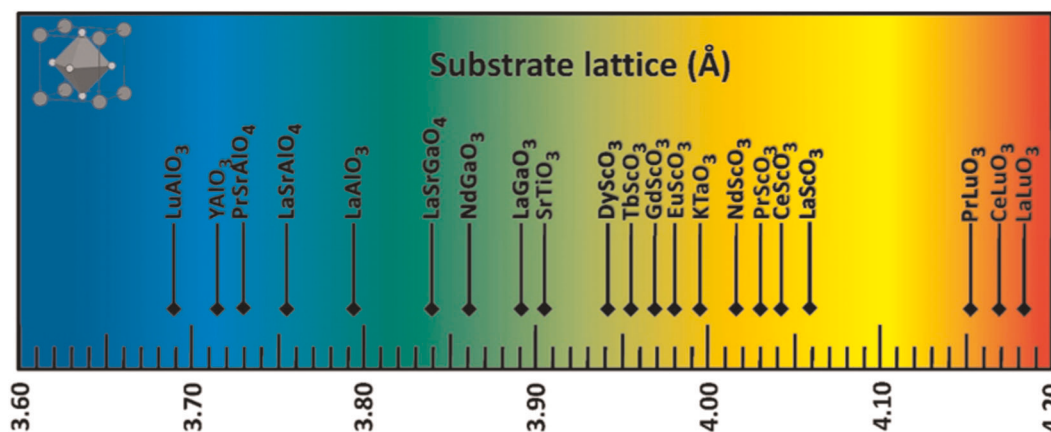


**Fig. 1** Typical substrates that are used in the growth of perovskite oxide thin-film and superlattice. Pseudo-tetragonal or pseudo-cubic lattice parameters (Å) for typical perovskite substrates, which include LuAlO<sub>3</sub><sup>69</sup>, YAlO<sub>3</sub><sup>63,70</sup>, PrSrAlO<sub>4</sub><sup>63</sup>, LaSrAlO<sub>4</sub><sup>63,71</sup>, LaAlO<sub>3</sub><sup>63,72</sup>, LaSrGaO<sub>4</sub><sup>63,73</sup>, NdGaO<sub>3</sub><sup>74,75</sup>, LaGaO<sub>3</sub><sup>74,76</sup>, SrTiO<sub>3</sub><sup>63,74</sup>, KTaO<sub>3</sub><sup>61,74,77</sup>, RScO<sub>3</sub><sup>61,74,77</sup>, and RLuO<sub>3</sub><sup>78,79</sup> ( $R$  represents the rare-earth element).

### Electric boundary condition: fixed applied electric field

For electronic device applications under short-circuit conditions<sup>44</sup>, the applied external electric field is an important electric boundary condition for perovskite superlattices. Under vanishing applied electric field  $\mathbf{E}=0$ , the spontaneous polarization ( $\mathbf{P}$ ) is a key property of FE material, which can now be routinely computed based on the modern theory of polarization<sup>80,81</sup>. The ionic contribution of polarization is straightforward, however, the electronic contribution should be computed via the Berry phase formulation given by  $\varphi_n = \text{Im}[\int d\mathbf{k} \langle u_{n\mathbf{k}} | \partial_{\mathbf{k}} | u_{n\mathbf{k}} \rangle]$ , in which the Bloch-like wavefunctions  $u_{n\mathbf{k}}$  from each occupied electronic band with index  $n$  over the Brillouin zone ( $\mathbf{k}$ ) are generated by the DFT ground state minimization<sup>81</sup>. In practice, the parallel transportation gauge is often adopted in the numerical implementation of the Berry phase calculation<sup>81</sup>. Moreover, important functional properties emerge in response to the applied finite electric fields in oxide superlattices, such as piezoelectricity or magnetoelectric couplings, in which the strong nonlinear effects were observed<sup>82</sup>. In order to properly treat the nonlinear responses, it is necessary to compute the electronic structure under the applied electric fields, which turned out to be nontrivial within the DFT framework<sup>83–86</sup>. The difficulty lies at the fact that the macroscopic electric field results in a change of the electric potential under a lattice vector translation, which breaks down the periodicity underlying Bloch's theorem and changes the qualitative character of the energy eigenstate<sup>87</sup>. In addition, an external electric field tilts the conduction and valence bands in real space. As a result, it always trends to lower the energy of a system with bandgap by transferring electrons from valence band of one region to a conduction band of another region with the distance, which is known as the Zener tunneling effect<sup>87,88</sup>. However, it was realized that the density matrix  $\rho(\mathbf{r}, \mathbf{r}')$  and other local quantities remain periodic under translation by a vector  $\mathbf{R}$  in the polarized ground state when the Zener tunneling is not significant under small applied electric fields. By imposing the periodicity in  $\rho(\mathbf{r}, \mathbf{r}')$ , Souza Ínguez, and Vanderbilt<sup>86</sup> proposed a practical approach to compute the "long-lived" electronic states under applied electric fields by minimizing the electric enthalpy functional  $F(\mathbf{E}) = E_{\text{KS}}(u_{n\mathbf{k}}) - \mathbf{E} \cdot \mathbf{P}$ . In the above,  $E_{\text{KS}}(u_{n\mathbf{k}})$  is the ordinary Kohn–Sham energy per unit volume under zero electric field,  $u_{n\mathbf{k}}$  is the periodic part of Bloch function, and the macroscopic polarization  $\mathbf{P}$  is composed by the ionic and electronic (Berry phase) contributions, respectively. To avoid a runaway solution associated with the Zener tunneling, a sparser  $\mathbf{k}$ -space mesh should be chosen with  $2\pi/\Delta k < E_g/|\mathbf{E}|$  in the practice calculation. As such, this method provides a first-principles computational framework to investigate many functional properties of materials under external electric fields.

### Electric boundary condition: fixed applied electric displacement field

Fixed electric displacement ( $\mathbf{D}$ ) field is another important electric boundary condition in which the functional materials are often studied by first-principles calculations. The importance is mainly due to two factors. One is that the DFT calculation under constrained  $\mathbf{D}$  field is directly corresponding to the open circuit condition for device applications<sup>44,89</sup>. Another factor is that first-principles studies under this electric boundary condition provides a powerful theoretical tool to probe the metastable states and to utilize the locality of FE oxide thin-films and superlattices. Unlike the paraelectric (PE) systems, the FE materials are strongly nonlinear materials. The equation of states, such as the electric polarization and electric enthalpy, are multivalued as a function of applied electric field. Therefore, one could only obtain the stable structure corresponding to the global minimum of electric enthalpy functional (see discussion in the section of "Electric boundary condition: fixed applied electric field") while the

metastable and unstable states of FE materials are not accessible by the same approach. Fortunately, the above difficulty can be overcome by adopting the constrained  $\mathbf{D}$  field in DFT calculations, in which the energy landscape  $U(\mathbf{D})$  becomes a single-valued function of  $\mathbf{D}$  field allowing the complete probing of energy landscape including both stable and metastable regions<sup>90–92</sup>. Moreover, the DFT calculations under constrained  $\mathbf{D}$ -field are particularly useful in the modeling and interface design rules for FE oxide superlattices. In insulating FE perovskite superlattices, both local polarization and local electric field vary in different layers<sup>44,89,93</sup>. However, the charge continuity principle ( $\nabla \cdot \mathbf{D} = 0$ ) ensures that the electric displacement vector  $\mathbf{D}$  is continuous along the growth direction, which is the [001] direction by convention. Therefore, the electric displacement field should be taken as the fundamental parameter that is uniform along the [001] direction, which has been conceptually proven for superlattice with continuous<sup>19,44</sup> or discontinuous polarity<sup>89,94</sup>. Furthermore, the force-constant matrix of the insulating perovskite superlattice becomes short-ranged under constrained  $\mathbf{D}$ -field. The locality principle enables one to extract the interface and bulk properties separately from the superlattices, which can be applied to inversely design perovskite superlattices of desired functional properties. Stengel et al.<sup>44</sup> have developed the fixed  $\mathbf{D}$ -field methodology within the DFT framework. It is achieved by minimizing the energy functional,  $U(\mathbf{D}, \nu) = E_{\text{KS}}(\nu) + \frac{\Omega}{8\pi} [\mathbf{D} - 4\pi\mathbf{P}(\nu)]^2$  where  $\Omega$  is the cell volume,  $E_{\text{KS}}$  is the ordinary zero-field Kohn–Sham energy functional, and  $\nu$  are the internal (both ionic and electronic) coordinates.

As one of the first applications, the DFT calculations with fixed  $\mathbf{D}$ -fields have been applied by Hong and Vanderbilt to successfully probe the complex energy landscape and equation of states of  $\text{PbTiO}_3$  (PTO)<sup>90,95</sup>. The energy enthalpies  $U(\mathbf{D})$  and  $F(\mathbf{E})$  along [001], [110], and [111] directions are computed as functions of electric displacement field  $\mathbf{D}$  and applied electric field  $\mathbf{E}$  in Fig. 2a, b, respectively. Clearly, it can be seen that energy functional  $U(\mathbf{D})$  is a single-value function of  $\mathbf{D}$  while energy functional  $F(\mathbf{E})$  is a multivalued function of  $\mathbf{E}$ . Therefore, the DFT calculations with fixed  $\mathbf{D}$ -fields can obtain not only the FE ground states with tetragonal symmetry as denoted by point 3 and 5 in Fig. 2a–c, but also the metastable states under applied (coercive) electric fields at point 2 and 4 as well as the unstable state at point 1 representing the hypothetical centrosymmetric phase of PTO with the  $P4/mmm$  space group symmetry. In stark contrast, DFT calculations with fixed- $\mathbf{E}$  electric boundary condition can only solve the equations of state for the stable and part of metastable regions; while the region 4→1→2 as shown in Fig. 2c, which has the negative dielectric permittivity  $\chi = \partial\mathbf{P}/\partial\mathbf{E}$  is unstable with respect to the applied electric fields and therefore it is inaccessible to the DFT calculation with fixed- $\mathbf{E}$  electric boundary condition. The authors also studied the structural stabilities of PTO as functions of  $\mathbf{D}$ -fields<sup>90</sup> by exploring the contour energy surface  $U(\mathbf{D})$  of PTO with respect to constrained  $\mathbf{D}$ -fields in both [100] and [010] directions. As shown in Fig. 2d, the four energy minima along  $\pm[001]$  and  $\pm[010]$  directions represent four of the six tetragonal ( $\mathbf{T}$ ) structures which are degenerate at DFT ground state; the four saddle points along [110] axis and the corresponding symmetry-equivalent directions depict the orthorhombic ( $\mathbf{O}$ ) phases. The energy barrier between  $\mathbf{T}$  and  $\mathbf{O}$  phases is significantly smaller than that between the  $\mathbf{T}$  phase and the centrosymmetric (paraelectric) phase at the origin. It indicates that it will be much easier to switch the electric polarization in a tetragonal PTO along the path connecting state  $\mathbf{T} \rightarrow \mathbf{O} \rightarrow \mathbf{T}$  than the path passing through the origin as shown in Fig. 2d. The contour energy surface  $U(\mathbf{D})$  as functions of constrained  $\mathbf{D}$ -fields along [110] and [001] direction is also computed as plotted in Fig. 2e. In addition to the global energy minima and local minima corresponding to the  $\mathbf{T}$  and  $\mathbf{O}$  phases, four extra saddle points are also identified which correspond to the rhombohedral ( $\mathbf{R}$ ) phase with the polarization

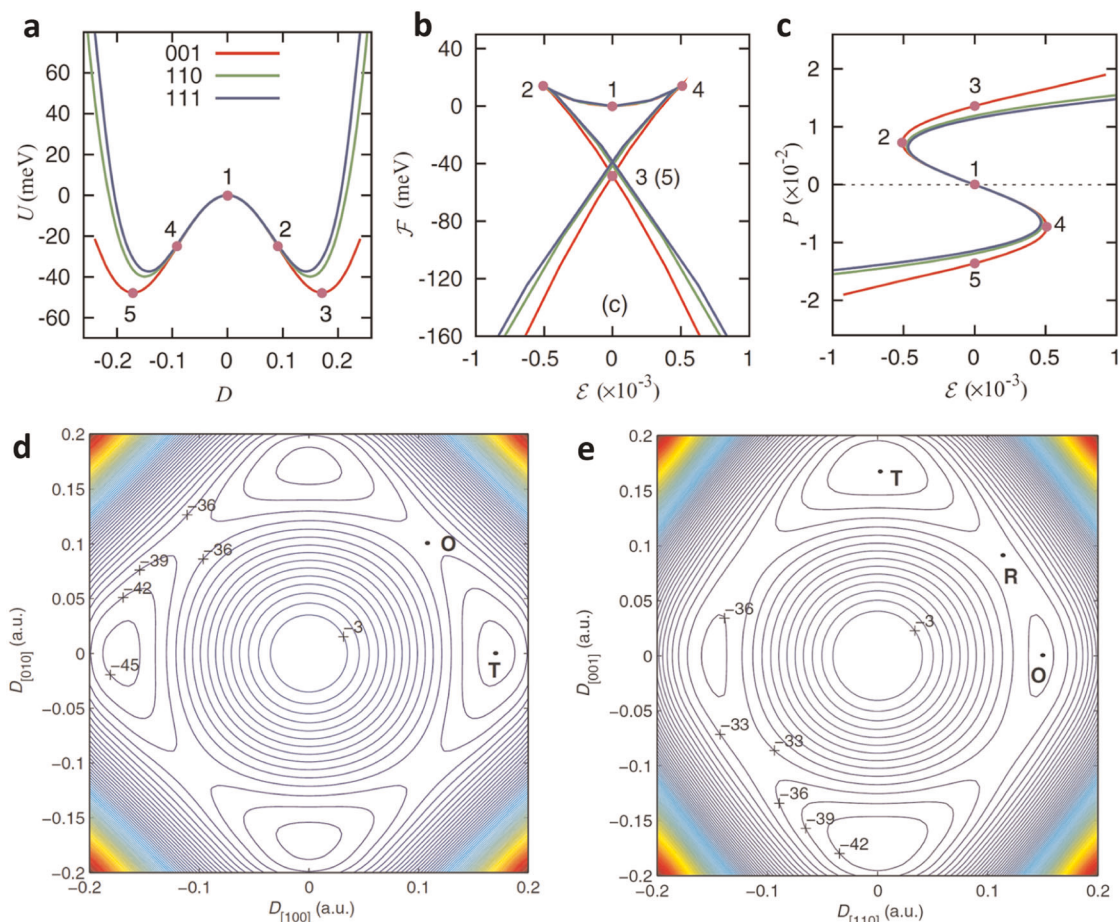


**Fig. 2** Energies computed by density functional theory in one typical ferroelectric oxide under constrained electric fields or constrained electric displacement fields. In  $\text{PbTiO}_3$  **a** energy  $U(D)$  as a function of electric–displacement ( $D$ ) and **b** energy  $F(\xi)$  as a function of electric-field ( $\xi$ ) of PTO along [001], [110], and [111] directions. **c** Electric polarization  $P(\xi)$  as a function of electric field  $P(\xi)$  along [001], [110], or [111] directions. **d** Electric Contour energy profile  $U(D)$  for  $D$  in the plane along the [100] and [010] directions. **e** Contour energy  $U(D)$  for  $D$  constrained in the plane determined by the [110] and [001] directions. All variables are in atomic units. In **d** and **e**, the minimum at **T** and saddle point at **O** represent tetragonal and orthorhombic states, respectively. Reproduced with permission from ref. <sup>90</sup>. Copyright [2011] {American Physical Society}.

along [111] or symmetry-equivalent directions. Similarly, polarization rotation from tetragonal phase to rhombohedral phase via  $\mathbf{T} \rightarrow \mathbf{R} \rightarrow \mathbf{O}$  path is found to be lower in energy compared to a direct switching through a paraelectric state at the origin. The small barriers connecting these minima with different orientations of polarization play a crucial role for the easy polarization rotation in PTO originating the large piezoelectric responses which has been predicted by previous theoretical studies<sup>96,97</sup>.

Besides the ability to probe complex energy profiles of FE materials, the DFT calculations with fixed- $D$  electric fields also provide a powerful scheme to explore the *locality* principles, which can be applied in the inverse design of oxide superlattices with desired functional properties. The perturbation in the electronic structure by the defects obeys the nearsightedness in the absence of long-range Coulomb interaction principle as shown by Prodan and Kohn<sup>98</sup>. In this scenario, the interface can be considered as an effective defect and should only affect the properties of oxide superlattice in a well localized region, where else is determined by its bulk property. The fixed electric displacement field provides such a framework in demonstrating such locality principle, in which the long-range electrostatic interaction can be described by the uniform  $D$  field. In several extensive studies, it has been shown that the both the perturbed electric and structural properties by the interfaces are indeed well localized<sup>19,99</sup>. The locality in polarization profile near the interfaces

has been demonstrated in perovskite superlattice facilitated by the layer polarization analysis<sup>100,101</sup>. Suppose the polarization is along the same direction of superlattice growth direction  $z$  or [001], the layer polarization of each AO (or  $\text{BO}_2$ ) charge neutral layer with index  $j$  is defined by<sup>19,101</sup>  $P_j = \frac{1}{S} \sum_{\tau \in j} Q_\tau R_\tau - \frac{2e}{S} \sum_{m \in j} Z_m$ . Note that the sum is confined to the ionic and Wannier centers belonging to layer  $j$ .  $\tau$  denotes ion cores with charge  $Q_\tau$  located at  $R_\tau$  and  $m$  denotes Wannier centers with charge  $-2e$  located at  $Z_m$  and  $S$  is the in-plane base area. The layer polarization  $p_j$  has units of dipole moment per unit area, and satisfies the sum rule, i.e., the total polarization is exactly equal to the sum of layer polarizations  $p_j = c^{-1} \sum_j p_j$  where  $c = V/S$  is the supercell lattice constant along  $z$  direction. The locality principle was evidenced by the fact that layer polarization as a function of  $D$  field  $P_j(D)$  strongly depends on the local compositional environment. More specifically as shown in the Fig. 3, the BaO layer polarizations in  $\text{SrTiO}_3(\text{STO})/\text{CaTiO}_3(\text{CTO})/\text{BaTiO}_3(\text{BTO})$  superlattices are mainly depended on the characteristic of the layer itself and its nearest layer chemical environment which are only weakly perturbed by the chemical environment of next nearest neighbors. Later, Swartz and Wu<sup>99</sup> have further shown that the local lattice deformation in terms of the layer height  $h_j(D)$ , defined by  $(\bar{Z}_{j+1} - \bar{Z}_{j-1})/2$ , where  $\bar{Z}_j$  is the average of  $z$ -coordinate ([001]) of all ions belonging to layer  $j$  basically shows the similar localized property as shown in Fig. 4. Later studies showed that other structural distortion such as the

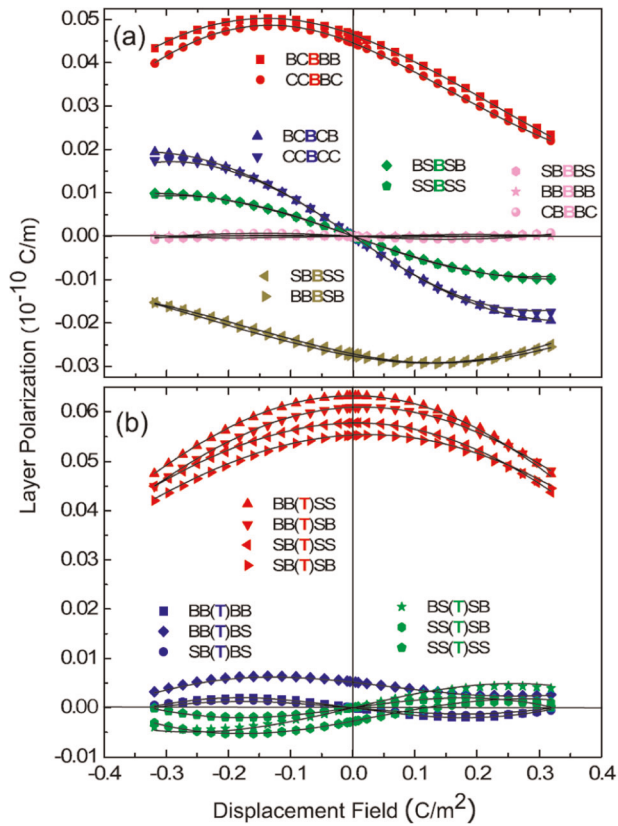


**Fig. 3 Localized electric property for a layer in a perovskite superlattices.** **a** Layer polarizations of BaO planes (relative to bulk BaTiO<sub>3</sub>) as functions of electric displacement field ( $D$ ) fields. **b** Layer polarizations of TiO<sub>2</sub> planes (relative to the average of layer polarization of TiO<sub>2</sub> planes in bulk BaTiO<sub>3</sub> and SrTiO<sub>3</sub>) as functions of electric displacement field ( $D$ ) fields. C, S, B, and T represent CaO, SrO, BaO, and TiO<sub>2</sub> layers, respectively. Results from first-principles calculations and model predictions are denoted by symbols and solid lines respectively. Reproduced with permission from ref. <sup>19</sup>. Copyright [2008] {American Physical Society}.

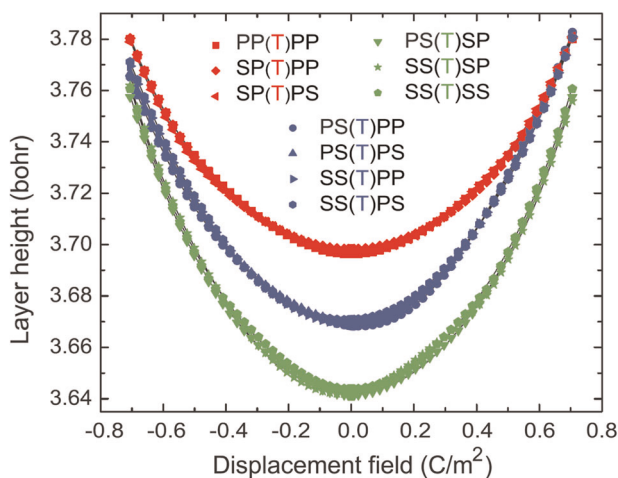


**Fig. 4 Localized lattice deformation for a layer in a perovskite superlattices.** Layer heights of TiO<sub>2</sub> in various chemical environments in PbTiO<sub>3</sub>/SrTiO<sub>3</sub> superlattices. P, S, and T denote PbO, SrO, and TiO<sub>2</sub> layers in the superlattices. Symbols and solid lines represent the results of first-principles calculations and model predictions, respectively. Reproduced with permission from ref. <sup>99</sup>. Copyright [2012] {American Physical Society}.

oxygen octahedral rotations and tilts<sup>8,102</sup> essentially follow the similar trend as described above. Such a locality principle has been utilized to build truncated cluster expansion model in order to accurately extract the electric and structural properties of interfaces as a function of  $D$  field. The above model is able to predict the electric, piezoelectric, and dielectric responses in superlattices with arbitrary sequences with an accuracy comparable to direct DFT calculation. Such a method paves the way to efficiently design oxide superlattice with desired functional properties.

### INDUCED OR ENHANCED FUNCTIONAL PROPERTIES UNDER EPITAXIAL STRAIN

Ferroelectricity in thin films under epitaxial strain

In terms of lattice dynamics, the proper FE can be described by the soft mode picture<sup>103–106</sup>. An unstable polar phonon mode at the Brillouin zone center freezes below the Curie temperature giving rise to the broken inversion symmetry with a lower symmetry. In conventional perovskite FE materials, such as BTO, PTO, and KNbO<sub>3</sub> (KNO)<sup>106</sup>, the development of FE mode represents a delicate balance of Coulombic interactions. Ghosez et al.<sup>107</sup> decomposed the interatomic forces into the contributions from long-range dipole–dipole interaction and those from short-range repulsive interaction. The former one originates from long-range electrostatic interaction and favors a polar distortion, while the latter is attributed to the repulsions between electrons on adjacent ions favoring the nonpolar centrosymmetric phase. Interestingly, these two interactions vary rather differently as a function of interatomic distance  $r$ . It was argued that<sup>108</sup> the short-range repulsion forces increase more rapidly with the  $r^{-n}$  dependence than the  $r^{-3}$  dependent long-range dipole–dipole counterpart while the interatomic distance  $r$  decreases under applied pressure, where  $n$  is a large number around 10<sup>108</sup>. This theory is consistent with the recent DFT calculation, in which it was found that FE disappeared in bulk BTO with the decreased interatomic distance when cell volume became smaller under applied external pressure<sup>96,107</sup>. This scenario is further evidenced by more recent first-principles calculations in which the short-range interatomic interaction was replaced by bulk BTO value, while the long-range dipole–dipole interaction is intact under applied high pressure. The series of calculations indicated that the polar instability becomes stronger due to the artificially suppressed short-range interatomic interactions<sup>107</sup>. Therefore, adjustment of the interatomic distance is an effective way in tuning the FE. It could be achieved by the epitaxial strain in thin-films and superlattices based on modern thin film technology.

The application of epitaxial strain has been widely adopted to modulate the FE instability in perovskite thin films. As one of the early applications, Choi et al.<sup>109</sup> have grown BTO thin films on substrates of GdScO<sub>3</sub> and DyScO<sub>3</sub>, which impose a compressive strain on BTO about  $-1.0\%$  and  $-1.7\%$ , respectively. As shown in Fig. 5, the compressive in-plane strain would elongate the lattice constant in  $c$ -axis, i.e., [001] direction. Under such mechanical boundary condition, the long-range dipole–dipole interaction is preferred relative to the short-range repulsion. As a result, the FE properties in these films are largely enhanced evidenced by the measured remnant polarization  $P_r$  of  $\sim 50 \mu\text{C}/\text{cm}^2$  and  $\sim 70 \mu\text{C}/\text{cm}^2$  on GdScO<sub>3</sub> and DyScO<sub>3</sub> substrate, respectively<sup>109</sup>, which are almost two or three times the value of  $\sim 26 \mu\text{C}/\text{cm}^2$  in natural bulk BTO. The enhanced FE in these compressed BTO thin-films are further supported by the enhanced FE structural phase transition temperature  $T_c$ , which were measured to be  $\sim 400^\circ\text{C}$  on GdScO<sub>3</sub> and  $\sim 540^\circ\text{C}$ <sup>109</sup> on DyScO<sub>3</sub>, respectively. These results demonstrated a significant increase in the structural phase transition temperature of  $\sim 130^\circ\text{C}$  in bulk BTO. Not only it could be used to enhance FE, the applied epitaxial strain can be even used to

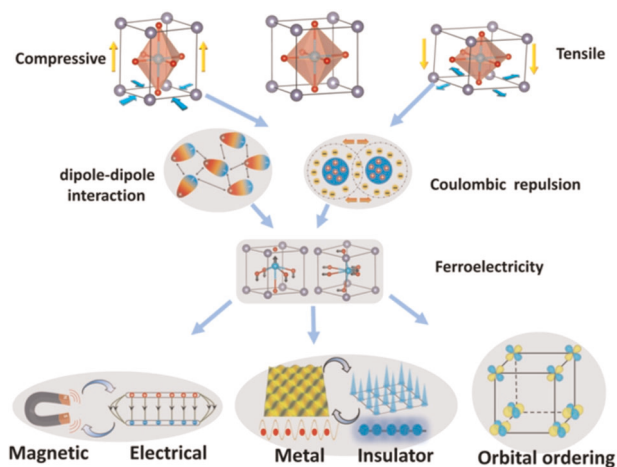


**Fig. 5 Functional properties of perovskite as ferroelectricity and its responses to external stimuli.** Schematic plots show the epitaxial strain effects on structure, magnetic, and electric properties of perovskite compounds.

induce FE in perovskite thin films that is PE in natural bulk format. For example, Zhang et al.<sup>110</sup> theoretically explored the induced FE under both compressive and tensile strains in BaZrO<sub>3</sub> (BZO), which has a centrosymmetric cubic structure in unstrained bulk state. Their first-principles calculations suggested that BZO can develop out-of-plane [001] polarization comparable to that of BTO under compressive strain slightly larger than  $-2\%$ ; when the applied compressive strain is further increased to  $-4\%$ , the induced FE polarization along [001] became as large as  $34 \mu\text{C}/\text{cm}^2$ , which is even larger than that of bulk BTO at room temperature. Under the tensile strain, their calculations further showed that an in-plane FE can develop. This is due to the elongated  $a$ - $b$  axes that promotes the long-range dipole-dipole interaction within the  $a$ - $b$  plane<sup>110</sup>.

In addition to its tunability on the magnitude of FE polarization, it was found that the orientation of polarization can also be effectively controlled as a function of the applied epitaxial strains<sup>111–113</sup>. Diéguez et al.<sup>111,112</sup> investigated the polar properties of several bulk perovskite oxides, including BTO, BZO, PTO, and KNbO<sub>3</sub>, etc. under epitaxial in-plane biaxial strains. The results are shown in Fig. 6. For all the structures considered, under sufficiently high compressive strain, the polarization always points towards the direction normal to the  $a$ - $b$  plane. Furthermore, applied tensile strain tends to develop a component of polarization within the  $a$ - $b$  plane. Due to the different FE directions that compressive and tensile strains promote, the resulting polarization vector is effectively rotated from [001] direction into in-plane direction when the epitaxial strain is gradually increased from compressive to tensile regions as shown in Fig. 6.

In the last section, we have mainly focused on the dependence of FE distortion on the applied epitaxial strains only. In those examples, applying epitaxial strains to thin-film perovskites is shown to be an efficient way to tune polarization in both the magnitude and the orientation. However, in the reality, other important structural distortions such as the antiferrodistortive (AFD) modes that associate with the oxygen octahedral rotations and tilts<sup>114–117</sup> can coexist with the FE distortion. Emergent phenomena appear when the complex energy landscape is nontrivially modified since the various structural distortions can have distinct dependence on the applied epitaxial strain<sup>114,118,119</sup>. For example, the lattice dynamics based on first-principles calculations showed that cubic STO is unstable under both polar and AFD distortions<sup>114,118</sup>. However, STO is only PE at all temperatures. The structure of STO is cubic at room temperature and transforms directly into tetragonal  $I4/mcm$  symmetry incorporating AFD distortion associated with oxygen octahedral

rotation around [001] axis below  $105 \text{ K}$ <sup>120,121</sup>. The absence of FE was attributed to the quantum fluctuation that suppresses the FE phase<sup>122</sup>. Furthermore, Monte-Carlo simulation studied by Zhong and Vanderbilt<sup>123</sup> showed that the polar distortion is further suppressed by the competition between AFD and FE instabilities. Nonetheless, the weak FE instability of bulk STO is very sensitive to external stimuli too. Based on Landau–Ginzburg–Devonshire theory, Pertsev et al.<sup>124</sup> investigated the effect of epitaxial strain on the structural properties of STO thin-film. The density of Helmholtz free energy  $F$  of STO was expanded in terms of order parameters and their couplings which included misfit strain, FE and AFD structural distortions. In their work, single-domain thermodynamic equations of state in STO films under various strain and temperature conditions were obtained by searching over all minima of  $F$  with respect to the components of both the FE and AFD distortions. Furthermore, the temperature dependent second-order coefficients were fitted by the Barrett formula<sup>125</sup> and then extrapolated to higher temperatures. From the determined most energetically favorable phases, it was shown that STO films can become FE under certain applied strain as temperature is reduced from room temperature. The induced FE is due to the coupling between the polarization and strain, which favors the polar distortion along out-of-plane (in-plane) direction under applied compressive (tensile) strain, respectively. These predictions using phenomenological model were also confirmed by first-principles calculations. Antons et al.<sup>126</sup> studied the effects of the in-plane epitaxial strains on the dielectric response and FE of STO films by DFT calculations. Under applied compressive (tensile) strains which are larger than critical values, the STO films were found to transform into tetragonal (orthorhombic) phase with polarization developed along [001] ([110]) direction. Experimentally, Yamada et al.<sup>127</sup> examined the in-plane and out-of-plane FE in a compressively strained STO film by reciprocal permittivity via infrared reflection spectroscopy. Based on spectral analysis, it was concluded that the in-plane polar mode softens very slowly; while the spectral signal clearly indicated that the FE structural phase transition associated with an out-of-plane polarization appears below  $\sim 150 \text{ K}$ , which is consistent with theoretical predictions<sup>126</sup>.

Let us take a look at another example. Ground state of CTO has a nonpolar orthorhombic structure with  $Pbnm$  symmetry<sup>119</sup>, which is transformed from the cubic structure ( $Pm\bar{3}m$ ) through mode combinations of both  $M_3^+$  and  $R_4^+$  associated with oxygen octahedral rotations around [110] and [001] directions, respectively. Besides these AFD structural instabilities, first-principles calculations also identified that cubic CTO also has a strong zone center polar instability ( $\Gamma_4^-$  mode)<sup>102,128,129</sup> as evidenced by the imaginary frequency around  $\sim 120i \text{ cm}^{-1}$ <sup>129</sup>. However, the development of FE distortion is inhibited in the ground state of CTO due to the strong competition between antipolar distortion ( $X_5^+$  mode) and polar distortion ( $\Gamma_4^-$  mode)<sup>28</sup>. Eklund et al.<sup>115</sup> studied structural properties of CTO under epitaxial strain by DFT calculations. The polar structures, with space group symmetries of  $Pmn2_1$  (polarization along  $a$ ) and  $Pmc2_1$  (polarization along  $b$ ), were found to be stabilized under tensile strains as shown in Fig. 7. In particular, the  $Pmn2_1$  structure can develop a large polarization of  $46 \mu\text{C}/\text{cm}^2$  under  $4\%$  tensile strain. Further analysis reveals that the oxygen octahedral rotations ( $M_3^+$  and  $R_4^+$  modes) as well as the antipolar distortion ( $X_5^+$  mode) are only little affected by the applied strains. Therefore, the induced FE in strained CTO films should mostly originate from the coupling between strain and polar instability as described above.

Multiferroic properties under epitaxial strain via spin-phonon coupling

In transition metal perovskites with open-shell cations on A or B sites, the magnetic exchange interactions are allowed by the  $f$  or  $d$  electrons. For example, in  $\text{EuMO}_3$  ( $M = \text{Ti, Zr, and Hf}$ ) with AFM

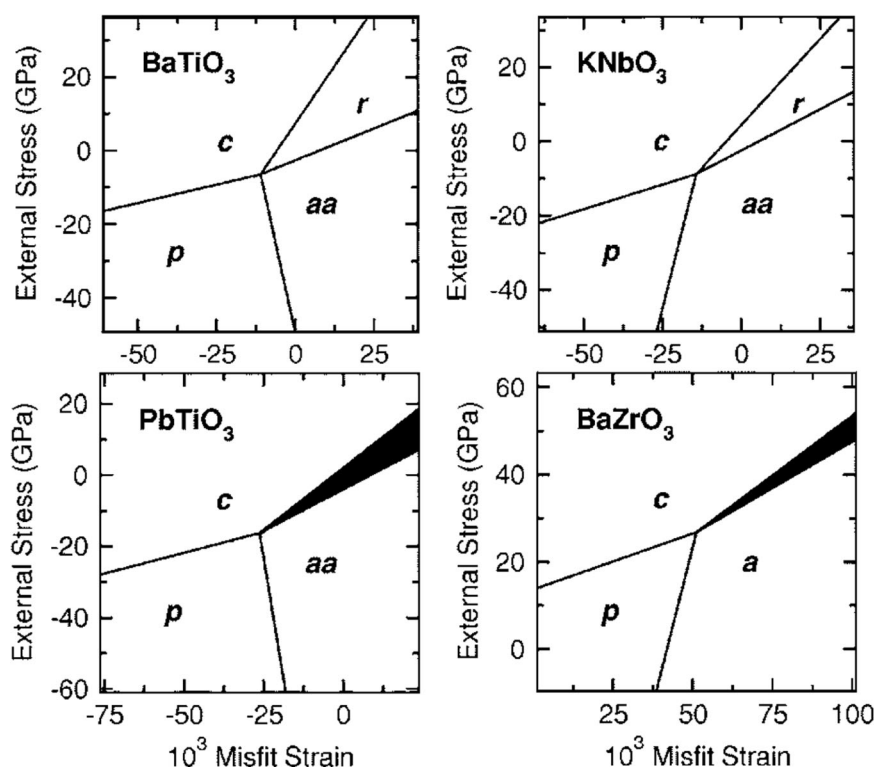


**Fig. 6 Tunable crystal structure in perovskites by external stress.** Phase diagram in  $\text{BaTiO}_3$ ,  $\text{PbTiO}_3$ ,  $\text{KNbO}_3$ , and  $\text{BaZrO}_3$  as functions of external stress and mismatch strain. *a*, *aa*, *r*, *c*, and *p* phases represent the perovskite structures with polarizations directed along  $[u00]$ ,  $[uu0]$ ,  $[uuv]$ ,  $[00v]$ , and  $[000]$  directions. Reproduced with permission from ref. <sup>111</sup>. Copyright [2005] {American Physical Society}.

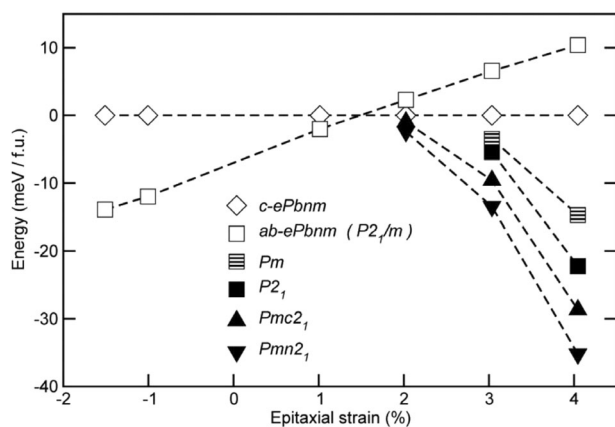


**Fig. 7 Structural phase transition under applied epitaxial strain in  $\text{CaTiO}_3$  determined by first-principles calculations.** The total DFT ground state energies of strained bulk  $\text{CaTiO}_3$  from first-principles calculations as a function of applied misfit strain. Reproduced with permission from ref. <sup>115</sup>. Copyright [2009] {American Physical Society}.

ground state, the superexchange interactions between neighboring *f* electrons of the  $\text{Eu}^{2+}$  cations are mediated through the *d* electrons of M cations<sup>130–132</sup>; whereas in AFM perovskites of  $\text{AMnO}_3$  (*A* = Ca, Sr, and Ba), the superexchange among *d* electrons of  $\text{Mn}^{4+}$  are facilitated by the *2p* orbitals of O anions<sup>42,43,133,134</sup>. The strength of the superexchange interaction is sensitive to the orbital hybridization determined by the bonding geometry<sup>42,43</sup>. Therefore, in multiferroic perovskites, the polar distortion that involves the magnetic cations potentially can be strongly coupled to the magnetic exchange interaction therefore spin orderings, which has been now known in the literature as the spin–phonon coupling effect<sup>14,42,43,134</sup>. Currently, the design of new multiferroic

materials by utilizing spin–phonon coupling is an active field. It is expected that artificial perovskites with AFM–PE ground state can be engineered into functional FM–FE state if the magnetic exchange interactions are sensitive to the low-lying polar mode that can be adjusted by the epitaxial strain.

The strain engineering via spin–phonon coupling was first proposed by Rabe and Fennie theoretically in  $\text{EuTiO}_3$ <sup>17</sup>. At room temperature,  $\text{EuTiO}_3$  is PM with a cubic structure of  $Pm\bar{3}m$  space group symmetry<sup>135,136</sup>. At low temperature, the magnetic moment of Eu cation adopts G-type AFM ordering below the Néel temperature of  $T_N = 5.5 \text{ K}$ <sup>137</sup>. From first-principles calculations, the spin–phonon coupling effect is evidenced by the softening of the  $\text{TO}_1$  polar phonon frequency about  $7 \text{ cm}^{-1}$  when magnetic ordering is constrained to be FM ordering. The strong spin–phonon coupling is further confirmed by the experimental observation in which the static dielectric constant in  $\text{EuTiO}_3$  undergoes significant increases as a function of increasing applied magnetic fields<sup>137</sup>. Its electronic origin is due to that the magnetic exchange interaction via the hybridization of Eu-*f* and Ti-*d* electrons are strongly coupled to the polar distortion. According to the theoretical investigations by Birol and Fennie<sup>131</sup>, the magnetic ordering in  $\text{EuTiO}_3$  is the competing results between the superexchange interaction and indirect exchange interaction which favor AFM and FM orderings, respectively<sup>138</sup>. The former involves the virtual electronic hopping processes between Eu-4*f* and Ti-3*d* orbitals, which is sensitive to Eu-*f* and Ti-*d* local bonding environment. The latter can be described by two consecutive processes. Firstly, an intra-atomic electron hopping process from 4*f* to 5*d* orbital occurs for the same Eu cation, which is barely affected by structural distortion; it is followed by the exchange interaction between two neighboring Eu cations favoring the FM state. Under the polar distortion, the Eu-*f* and Ti-*d* hybridization environments are suppressed resulting in decreased superexchange interactions. On the other hand, the indirect exchange interaction favoring FM ordering is mostly determined by the

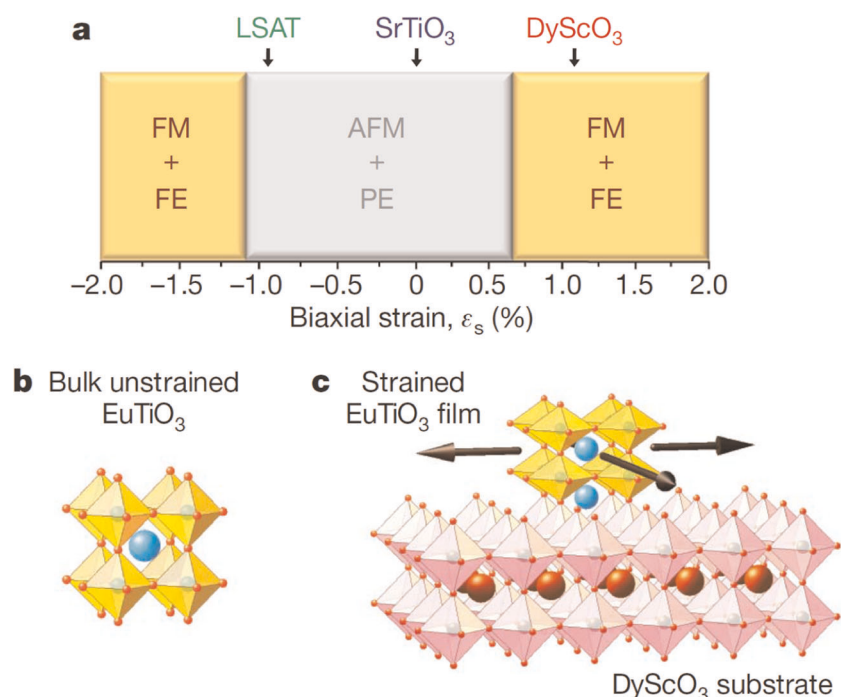


**Fig. 8 Multiferroic phases induced by epitaxial strain in  $\text{EuTiO}_3$ .** **a** Predicted phase diagram of strained  $\text{EuTiO}_3$  films with the biaxial strain ranging from  $-2\%$  to  $+2\%$ . **b, c** The ball-and-stick models of bulk  $\text{EuTiO}_3$  and epitaxially strained thin-film  $\text{EuTiO}_3$  on the  $\text{DyScO}_3$  substrate respectively. Reprinted with permission from ref. <sup>56</sup>. Copyright (2010) Springer Nature.

distance between two  $\text{Eu}^{2+}$  cations only and less sensitive to the polar mode. As a result, polar distortion tends to drive  $\text{EuTiO}_3$  from AFM–PE state to FM–FE state. Strain engineering in  $\text{EuTiO}_3$  was proposed by Fennie and Rabe<sup>17</sup> based on DFT calculations. Their calculations revealed that the infrared active  $\text{TO}_1$  polar phonon mode is strongly coupled with both magnetic ordering and epitaxial strain as described above. When the applied epitaxial strain is larger than  $1.25\%$  the ground state of  $\text{EuTiO}_3$  strained thin-film will become FM–FE via the spin–phonon coupling effect. By using the same mechanism, they argued that FM–FE state can also be stabilized by applied magnetic field or electric field, which are estimated to be  $1\text{ T}$  and  $10^5\text{ V/cm}^{-1}$ , respectively<sup>17</sup>. Later, the predictions were confirmed by experiments for an  $[001]$ -oriented  $\text{EuTiO}_3$  film grown on  $\text{DyScO}_3$  substrates by reactive molecular beam epitaxy technique<sup>56</sup>. The  $\text{DyScO}_3$  substrate exerts about  $+1.1\%$  biaxial strain on  $\text{EuTiO}_3$  film, which is close to the theoretically predicted critical strain to reach the FM–FE ground state as shown in Fig. 8. Temperature-dependent second harmonic generation measurements indicated that the  $\text{EuTiO}_3$  film exhibits a PE to FE transition at  $250\text{ K}$ . The temperature dependence of a magneto-optic Kerr effect shows that the same strained  $\text{EuTiO}_3$  has a clear FM hysteresis loop under the Curie temperature of  $4.24\text{ K}$ .

Despite the above success, the practical application in strained  $\text{EuTiO}_3$  films is still limited by the extremely low Néel temperature<sup>56</sup>. The weak magnetic exchange energy is partially due to the fact that  $f$  electrons of  $\text{Eu}^{2+}$  are screened by  $5s$  and  $5p$  electrons in outer shells<sup>130,138</sup>. While transition metal oxide perovskite, whose AFM magnetic ordering temperature governed by the superexchange interactions, can have much higher magnetic ordering temperatures, e.g., the Néel temperature in  $\text{SrMnO}_3$ <sup>15,42</sup> and  $\text{CaMnO}_3$ <sup>134</sup> are as high as  $260$  and  $130\text{ K}$ , respectively. In transition metal perovskites, the superexchange interactions involve the  $d$  electrons hopping processes between neighboring B-site cations, which are facilitated by the hybridization between cation  $d$  and oxygen  $2p$  orbitals. The resulting magnetic ground state prefers the AFM (FM) spin ordering when the B–O–B bond angle is close

to  $180^\circ$  ( $90^\circ$ ), which is the phenomenological rule proposed by Goodenough, Kanamori, and Anderson<sup>139–141</sup>. First-principles calculations revealed that polar modes in  $\text{AMnO}_3$ , such as the Slater mode in  $\text{SrMnO}_3$ , have a large projection on the B–O–B bond, which induced strong spin–phonon coupling effect<sup>42,43,134</sup>. Therefore, one can expect that the AFM–PE ground state in many transition metal perovskites can be potentially engineered to be FE–FM state by the epitaxial strain through the spin–phonon coupling.  $\text{SrMnO}_3$  is a prototypical transition metal perovskite with large spin–phonon coupling, which was evidenced by the softening of Slater phonon mode from  $121$  to  $109\text{ cm}^{-1}$  in cubic  $\text{SrMnO}_3$  from constrained G-AFM and FM spin orderings. Lee and Rabe<sup>15</sup> theoretically investigated the electronic and magnetic properties in  $\text{SrMnO}_3$  films under various applied epitaxial strains. It was found that the tensile strain higher than  $1\%$  transforms  $\text{SrMnO}_3$  from the PE/G-AFM ground state of  $Imma$  symmetry to the FE/G-AFM state of  $Ima2$  symmetry with the in-plane FE polar distortion ( $\Gamma_4^- [110]$ ). As the applied tensile strain further increases, the  $\Gamma_4^- [110]$  polar distortion continues to increase as shown in Fig. 9; meanwhile the magnetic ordering gradually changes from G-AFM to FM. The G-AFM phase with full anti-parallel spins on Mn cations is stable when the tensile strain is less than  $2.0\%$ . The C-AFM phase with about one-third parallel spins on Mn cations is energy favorable for the tensile strain range from  $2$  to  $2.8\%$ . The magnetic ordering further transforms to A-AFM at the tensile strain range from  $2.8$  to  $3.4\%$ , with two-third parallel spins on Mn sites. Finally, the FM–FE phase becomes the ground state as the tensile strain is larger than  $3.4\%$ . In their studies,  $\text{SrMnO}_3$  films can also be driven into FM–FE ground state of  $I4cm$  under compressive epitaxial strain as large as  $-2.9\%$ , in which the FE distortion ( $\Gamma_4^- [001]$ ) is along out-of-plane direction. Interestingly, no intermediate phase was identified between PE–AFM and FE–FM under the compressive epitaxial strains.

#### Tunable band gap under epitaxial strain

In open shell transition perovskites, the bandgap sometimes is closely associated with the onsite Coulomb interaction  $U$  and one-

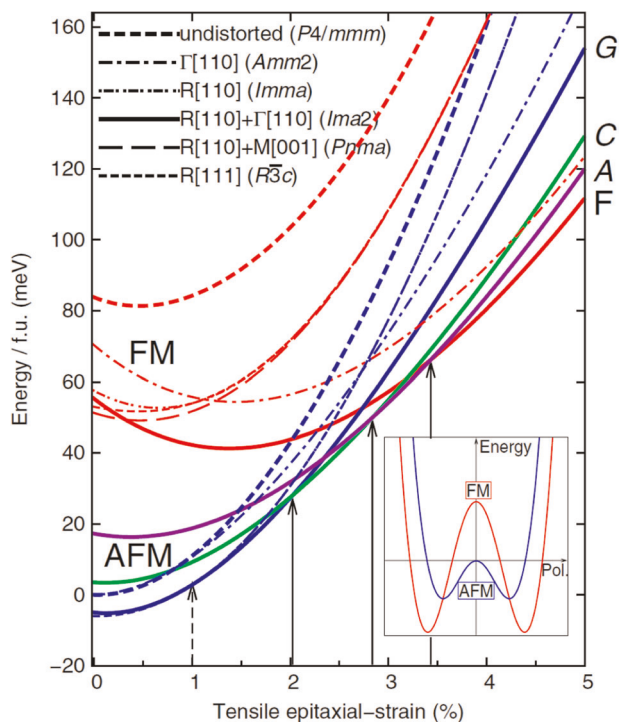


**Fig. 9 Multiferroic phases induced by epitaxial strain in SrMnO<sub>3</sub>.** The total DFT ground state energies as functions of applied tensile epitaxial strains in SrMnO<sub>3</sub>. Reproduced with permission from ref. <sup>15</sup>. Copyright [2010] {American Physical Society}.

electron bandwidth  $W$  spanning the highest-occupied and lowest-unoccupied  $d$  orbitals near Fermi energy such as SrCoO<sub>3</sub>. Roughly speaking, when  $U > W$ , an energy lowered by delocalizing electrons is unable to overcome the Coulomb blockade between neighboring sites, resulting in an insulator with band gap  $\approx U - W$ ; while for  $U < W$ , system is often found to be metallic<sup>142,143</sup>. Comparing to the relatively insensitivity of  $U$  on the structural distortion, the bandwidth  $W$  is proportional to degree of hybridization of  $d$ -orbital at transition metal atom and  $p$ -orbital at an adjacent oxygen atom, which is very sensitive to its bond length and angle<sup>43,142,143</sup>. Therefore, the applied epitaxial strain offers an opportunity to adjust the bandwidth  $W$  as well as the band gap in these transition metal perovskites. In particular, the crystal fields that arises from the electrostatic interaction between  $3d$  and  $2p$  orbitals can be adjusted via the polar distortion which changes the relative displacement between B-site atoms and their surrounding ligands. The subsequently rearranged energy levels can be used to tailor electronic states near Fermi level<sup>144–146</sup>.

The bandgap tunability in SrCoO<sub>3</sub> has been studied by Lee and Rabe<sup>16</sup> via first-principles calculations. SrCoO<sub>3</sub> has the cubic  $Pm\bar{3}m$  symmetry at ground state which is FM below the Curie temperature  $T_c \sim 305$  K. The FM ordering was found to be due to the double exchange interaction that strongly depends on the  $d$ - $p$  hybridization, whose strength is maximized for a 180° Co–O–Co bond angle. The strength of the double exchange is decreased in a restricted G-type spin configuration which is accompanied by the development of polar distortion<sup>147,148</sup>. At the same time, the zone center polar phonon also undergoes a dramatic softening from FM to G-AFM driven by the strong spin-phonon coupling. Since the electronic structure of SrCoO<sub>3</sub> near the Fermi energy is composed of the Co- $3d$  and O- $2p$  bands<sup>149</sup>, the bandwidth is largely affected by a FE distortion induced by the applied epitaxial strain. Considering the fact that the bandwidths of AFM and FM orderings are proportional to  $t^2/U$  and  $t$ , respectively<sup>150</sup>, where  $t$  is the hopping integral between two orbitals and in general,  $t$  is

greater than  $t^2/U$ . Therefore, the bandwidth is also decreased for the magnetic ordering changing from FM to AFM state. As a result, SrCoO<sub>3</sub> tends to have a finite band gap in the AFM state. The above scenario is consistent with the discoveries by first-principles calculations. Lee and Rabe<sup>16</sup> found that the metallic FM–PE SrCoO<sub>3</sub> transforms into insulating G-AFM–FE multiferroic phase when the applied epitaxial compressive and tensile strains are greater than  $-0.7\%$  and  $3.2\%$ , respectively. The origin of metal–insulator transition was proposed to be due to the bandwidth control via strain induced FE distortion as well as the influence from the magnetic ordering. At the phase boundary of  $-0.7\%$ , its lattice constant shows up a  $6.4\%$  jump. Simultaneously polarization jumps from 0 to  $\sim 30 \mu\text{C}/\text{cm}^2$ , and bandgap changes from 0 to 0.23 eV. Varignon et al.<sup>151</sup> recently proposed a different approach to tune the band gap by adjusting the electron orbital orderings through the indirect coupling between epitaxial strain and Jahn–Teller distortions. Jahn–Teller distortion is a common structural distortion that occurs in transition metal perovskites<sup>146</sup>. In response to the crystal field, the electronic degeneracy is lifted by the elongation or contraction of chemical bonds between the transition metal ion and its surrounding ligands as schematically shown in Fig. 10, which also lowers the energy. The Jahn–Teller distortion itself is nonpolar, therefore it is not directly coupled to the external electric field. Interestingly, the authors reported an indirect Jahn–Teller distortion and epitaxial strain coupling mechanism. It was realized by the anharmonic lattice couplings between polar mode in bulk perovskite with  $Pb2_1m$  symmetry and Jahn–Teller distortion. The  $Pb2_1m$  symmetry is not common in bulk perovskites, but it can be stabilized via strain engineering to active a silent polar mode as shown in Fig. 10. They studied four highly strained perovskites which are SrTiO<sub>3</sub>, BaMnO<sub>3</sub>, BiFeO<sub>3</sub>, and YMnO<sub>3</sub> respectively. In SrTiO<sub>3</sub>, BaMnO<sub>3</sub>, and BiFeO<sub>3</sub>, splitting between the  $t_{2g}$  states were observed near the Fermi energy. The tensile strain increases (decreases) the in-plane (out-of-plane) distance between central transition metal ion and its surrounding oxygen anions. As a result, the crystal field level of  $d_{xy}$  orbital is lower than that of  $d_{zx}$  and  $d_{yz}$  orbitals, which displays the electronic ordering with a predominant occupation of the  $d_{xy}$  state. Similarly, Jahn–Teller distortion in YMnO<sub>3</sub> lifts the  $e_g$  orbital degeneracy and displays an orbital ordering and predominantly occupation of  $d_{x^2-y^2}$  orbital, which widens band gap under moderate electric field.

#### Interface induced functional ferroelectric and multiferroic properties

With the development of advanced epitaxial engineering techniques, layer-by-layer epitaxial synthesis of perovskite-based multi-component superlattices has been made possible<sup>152,153</sup>. This enables the experimentalists to precisely control thickness as well as the order of the constituent layers along stacking direction. As illustrated in Fig. 11, the dissimilar lattice parameters, chemical environments, electrostatic potentials, and structural instabilities belonging to individual bulk constituents can lead to diverse physical interplays at the interfaces<sup>154–156</sup>. For instance, broken inversion symmetry can be designed by the species of perovskites in multicomponent superlattices<sup>13</sup>, which has a significant effect on FE properties<sup>1,157,158</sup>. Furthermore, electrostatic coupling between constituent layers in superlattices are mediated by the interfaces<sup>159</sup>, which tends to minimize the polarization mismatch of the constituent components in order to avoid large electrostatic energy penalty<sup>24</sup>. The effect of electrostatic coupling is now routinely being applied to tune FE in multicomponent superlattices for desired polarization. In addition, emergent polar structural distortions appear on the interface as a result of competing structural instabilities among parent perovskites<sup>160–162</sup>. In the above, structural distortions associated with octahedral rotations and tilts play important roles in FE properties of

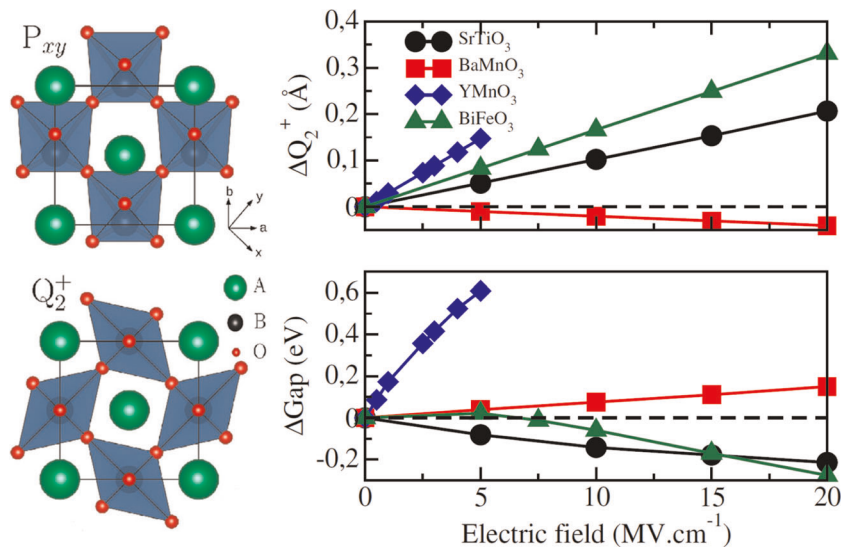


**Fig. 10 Tunable bandgap under applied electric field in perovskite via Jahn–Teller distortion.** Jahn–Teller distortion (top right panel) and bandgaps (bottom right panel) as a function of applied electric field in SrTiO<sub>3</sub>, BaMnO<sub>3</sub>, YMnO<sub>3</sub>, and BiFeO<sub>3</sub>. The atomic displacements associated with polar and Jahn–Teller distortions are schematically shown on the top and bottom right panels respectively. Reproduced with permission from ref. <sup>151</sup>. Copyright [2016] {American Physical Society}.

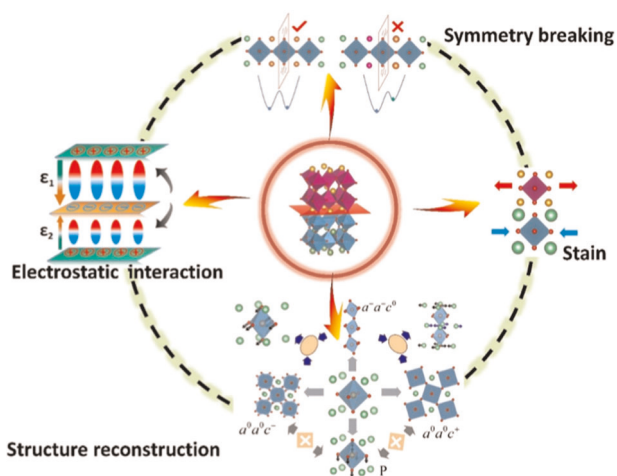


**Fig. 11 Thin-film engineering approaches that induce or enhance ferroelectricity in perovskite thin-film and superlattices.** Figure schematically shows that the ferroelectric polarization can be induced or enhanced by applied external strain as discussed, chemical compositions that breaks inversion symmetry in tricolor superlattices, electrostatic interaction mediated by the interfaces in the superlattices, and structural reconstruction associated with oxygen octahedron, which are discussed in the section of “Ferroelectricity in thin films under epitaxial strain”; “Compositional inversion symmetry breaking”; “Electrostatic coupling effect via interfaces”; and “Interfacial reconstructions of structural instabilities”; respectively.

perovskites<sup>163,164</sup>. Along this line, successful tuning of the amplitude even reconstructions of the oxygen octahedral rotations have been demonstrated recently<sup>165–168</sup> through the modified chemical pressure<sup>169</sup> (ionic radius and chemical bonding) at the interface. In this section, we first focus on the FE induced by compositional breaking of inversion symmetry; next, we summarize FE enhancement in recent literature by utilizing the electrostatic coupling effect via the interfaces; subsequently, we briefly review the mechanism of hybrid improper FE and its application in perovskite superlattices<sup>26,170</sup>; finally, we discuss the recent developed method to stabilize the highly polar FE phase on

the interfaces through the reconstruction of oxygen octahedral rotations.

#### Compositional inversion symmetry breaking

For artificial perovskite superlattices, it was realized<sup>22</sup> that the number of distinct species of parent perovskites, often referred as *colors*, can be used to break the inversion symmetry. The mechanism of broken inversion symmetry can be conveniently demonstrated by the interface dipole  $\mathbf{p}_{\text{int}}(\mathbf{D}) = \sum_i \mathbf{p}_i(\mathbf{D}) - \mathbf{p}_i^0(\mathbf{D})$ , in which  $\mathbf{p}_i(\mathbf{D})$  is actual *i*th layer polarization and  $\mathbf{p}_i^0(\mathbf{D})$  is a polarization of bulk constituent in that interface layer. As schematically shown in Fig. 12, the interface dipole must sum up to be zero to keep the inversion symmetry in bicolor superlattices; however, for the tricolor or multicolor superlattices with at least three species of perovskites, the sum of interface dipoles is nonzero due to the compositional symmetry breaking. It was proposed that the resulting self-poling effect could be used to enhance functionalities such as piezoelectricity in perovskite superlattices.

The inversion symmetry breaking in tricolor superlattice was proposed theoretically by Sai et al.<sup>13,157</sup>. They have performed ground state DFT calculations for artificial ternary perovskite superlattices of  $(A_{1/3}A'_{1/3}A''_{1/3})\text{BO}_3$  and  $A(\text{B}_{1/3}\text{B}'_{1/3}\text{B}''_{1/3})\text{O}_3$  by assuming [001] as the superlattice growth direction. In their studies, BTO has been chosen as the parent perovskite. Specifically, they considered two model systems, the first system is isovalent substitutions on both A and B sites in  $(\text{Ba}_{1/3}\text{Sr}_{1/3}\text{Ca}_{1/3})\text{TiO}_3$  and  $\text{Ba}(\text{Ti}_{1/3}\text{Zr}_{1/3}\text{Hf}_{1/3})\text{O}_3$ , respectively, and in the second system, they consider heterovalent substitution on the B site element in  $\text{Ba}(\text{Sc}_{1/3}\text{Ti}_{1/3}\text{Nb}_{1/3})\text{O}_3$ . The compositionally induced inversion symmetry breaking can be clearly identified by the asymmetric FE double well potentials from the DFT calculations as shown in Fig. 13. By using energy difference between the minimum of the two wells, it was found that the induced asymmetry in the heterovalent chemical substitution systems is much larger than that in the isovalent substitution systems. It indicates a larger magnitude of inversion symmetry breaking in the former. To better understand it, a pseudo-lattice model system  $\text{Ba}(\text{B}_{1/3}\text{Ti}_{1/3}\text{B}''_{1/3})\text{O}_3$  was built by the construction of artificial elements B and B'' with fractional nuclear charges  $\text{Ti} - \delta$  and  $\text{Ti} + \delta$ , respectively, which allows the gradual change of the

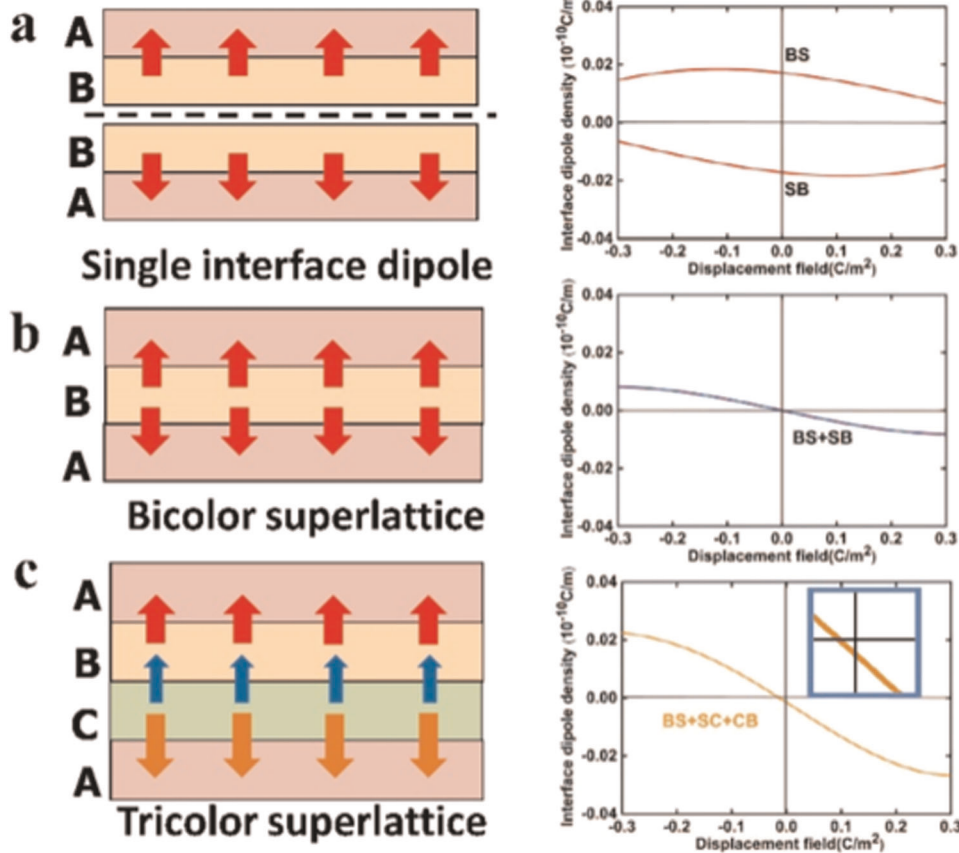


**Fig. 12 Broken inversion symmetry and induced ferroelectricity in the tricolor perovskite superlattice.** Schematic plots demonstrate how the spatial inversion is broken by the number of species (colors) included in the superlattice. **a** The individual interface dipoles and the **b** overall interface dipole as a function of electric displacement field in bicolor BaTiO<sub>3</sub>/SrTiO<sub>3</sub> bicolor superlattice. **c** The overall interface dipole as a function of electric displacement field in tricolor BaTiO<sub>3</sub>/SrTiO<sub>3</sub>/CaTiO<sub>3</sub> superlattices.

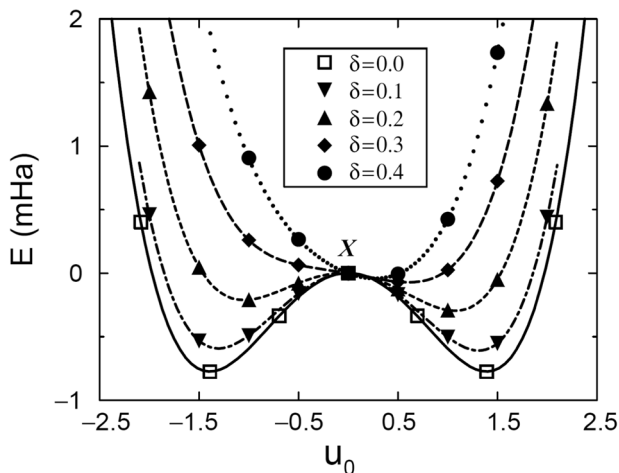


**Fig. 13 Tilted double well potential in tricolor perovskite superlattice.** The ferroelectric double well potentials as functions of charge perturbation  $\delta$  through the heterovalent substitution. Reproduced with permission from ref. <sup>13</sup>. Copyright [2006] {American Physical Society}.

heterovalent symmetry-breaking through the perturbation  $\delta$  deviating from that of Ti ( $Z = 22$ ). It was found that the strength of the symmetry breaking is very sensitive to the variation of  $\delta$  in Fig. 13, which shows a cubic dependence. Such a sensitive dependence of the inversion symmetry breaking on the charge

perturbation indicates that the FE and large piezoelectricity could be induced in tricolor superlattice which are only PE in bulk.

The compositional symmetry-breaking in tricolor superlattices has been confirmed later in experiments<sup>1,22</sup>. Warusawithana et al. had grown CTO/STO/BTO tricolor superlattices using molecular beam epitaxy on STO substrates. They found a strong asymmetrical dielectric response due to compositional symmetry breaking<sup>22</sup> based on the measured real part of the dielectric constants  $\epsilon'$  in (CTO)<sub>1</sub>(STO)<sub>1</sub>(BTO)<sub>2</sub>(STO)<sub>1</sub>(CTO)<sub>1</sub> and (CTO)<sub>2</sub>(BTO)<sub>4</sub>(STO)<sub>2</sub> superlattices, respectively. The inversion symmetry of the former is not broken by chemical composition, therefore the measured  $\epsilon'$  is an even function under the applied electric fields. On the other hand, the mirror symmetry of measure  $\epsilon'$  in (CTO)<sub>2</sub>(BTO)<sub>4</sub>(STO)<sub>2</sub> superlattice is broken as expected. At almost the same time, Lee et al.<sup>1</sup> also successfully grew a series of CTO/STO/BTO tricolor FE superlattices via the pulsed laser deposition technique. Significantly enhanced polarization was observed in some superlattices. Among the above, (STO)<sub>2</sub>(BTO)<sub>4</sub>(CTO)<sub>2</sub> sequence was found to have the maximum polarization<sup>1</sup>. For this particular superlattice, the remnant polarization is determined to be 16.5  $\mu\text{C}/\text{cm}^2$  in experiments showing roughly 50% enhancement compared the estimated values based on electrostatic model.

A few years later, the compositional inversion symmetry breaking design method has been also applied on multiferroic artificial materials. At bulk level, both LaMnO<sub>3</sub> and SrMnO<sub>3</sub> are PE insulators with G-AFM ordering, in which the Mn atoms adopt  $t_{2g}^3 e_g^1$  and  $t_{2g}^3 e_g^0$  electronic configurations respectively. As detected by the superconducting quantum interference device

magnetometer, FM ordering emerges at the interfaces of artificial  $\text{LaMnO}_3/\text{SrMnO}_3$  superlattice arising from the promoted double-exchange interactions from the charge-transfer between the  $e_g$  orbitals of  $\text{LaMnO}_3$  and  $\text{SrMnO}_3$ . Due to its bicolor nature, the space inversion symmetry remains unchanged in  $\text{LaMnO}_3/\text{SrMnO}_3$  system. Kida et al. designed the tricolor superlattice composed of  $\text{LaMnO}_3$ ,  $\text{SrMnO}_3$ , and  $\text{LaAlO}_3$  that breaks the inversion symmetry<sup>158,171</sup>. In such a superlattice space-inversion and time-reversal symmetries are both broken. Therefore, it possesses a toroidal moment defined as  $\mathbf{P} \times \mathbf{M}$ , where  $\mathbf{P}$  and  $\mathbf{M}$  denote the polarization and magnetization, which allows the nonvanishing magnetoelectric tensor  $a_{ij}$ . The real and imaginary parts of  $a_{ij}$  are associated with the directional refraction and absorption of light intensity, respectively<sup>172,173</sup>. The reversal of one of  $\mathbf{P}$ ,  $\mathbf{M}$ , or light wavevector  $\mathbf{k}$  (parallel or antiparallel to the toroidal moment) will result in a sign change of  $a_{ij}$  to modulate the refractive and absorptive light intensity, which is referred to as the optical magnetoelectric effect. The change of refractive light intensity was successfully detected in the  $\text{LaMnO}_3/\text{SrMnO}_3/\text{LaAlO}_3$  tricolor sample by a reversal of the direction of magnetic field<sup>171,172</sup>.

#### Electrostatic coupling effect via interfaces

The polar distortion is sensitive to the external electric fields. The electrostatic interaction generated by the uncompensated polarization charges at the interfaces provides an effective method to tune the FE instability in perovskite superlattices. At the interface of insulating superlattice, the electric displacement field,  $\mathbf{D} = \epsilon_0 \mathbf{E} + \mathbf{P}$ , must be continuous along the stacking direction of the superlattice, which is known to be the electric boundary condition as discussed in the section of "Electric boundary condition: fixed applied electric displacement field". In general, the polarization mismatch between the two constituent components will build polarization charge  $\nabla \cdot \mathbf{P}$  at the interfaces and lead to large energy cost<sup>24,46</sup>. In order to minimize the above electrostatic energy, the polarization mismatch should be reduced. In the FE/PE superlattices, the process is achieved by polarizing (depolarizing) the PE (FE) component through the long-range electrostatic interactions. As a result, a rather uniform local polarization profile instead of larger polarization mismatch forms in the superlattice along the stacking direction<sup>24,174–182</sup>. In the case of bicolor FE/PE superlattices, if one chooses the incipient FE perovskite (sch as  $\text{SrTiO}_3$  and  $\text{KTaO}_3$ ) as the PE component, the FE can be induced or recovered by the poling effect via the interfaces. The electrostatic coupling mechanism has been widely applied in the design of FE or multiferroic perovskite superlattices in the last decade<sup>8,24,25,183–187</sup>.

Polarization enhancement by electrostatic coupling was first demonstrated by Neaton and Rabe<sup>24</sup> in the epitaxial BTO/STO superlattices. They carried out DFT calculations for several five-period superlattices with the compositions of 4BTO/1STO, 3BTO/2STO, 2BTO/3STO, and 1BTO/4STO assuming the coherent growth on a STO substrate, as well as the bulk STO and strained bulk BTO. The space group symmetry  $P4mm$  of room temperature BTO is assumed for all the superlattices, which allows the development of polar distortions along superlattice growth direction. Without considering the electrostatic coupling effect, the overall polarization can be roughly estimated by the average over the polarization of each bulk constituent and its volume fraction in the superlattice. Since STO is PE, the estimated polarization should be therefore roughly proportional to the volume fraction of the BTO component. Surprisingly, the calculated polarizations of the superlattices by DFT are much larger than the above estimated value. In order to elucidate the underlying origin of the enhanced polarization in BTO/STO superlattice, the local polarization profile is computed based on the linear approximation as shown in Fig. 14a. Interestingly, the local polarization induced in STO layers is found to be comparable to that in BTO layers. Clearly, the discrepancy between the estimated and computed polarization suggested that the interface effect is very large. In order to quantitatively study the electrostatic coupling effect via the interface, a *dielectric slab* model was then proposed by Neaton et al.<sup>24</sup>. Within the *dielectric slab* model, short circuit boundary condition is applied by the vanishing total potential drop across the superlattice by  $\mathbf{E}_{\text{BTO}} \ell_{\text{BTO}} = -\mathbf{E}_{\text{STO}} \ell_{\text{STO}}$ , in which  $\mathbf{E}_{\text{BTO}}$  and  $\mathbf{E}_{\text{STO}}$  are the electric fields within the BTO and STO layers, respectively and the  $\ell_{\text{BTO}}$  and  $\ell_{\text{STO}}$  denote the layer thicknesses of BTO and STO respectively. Based on this model, the resulting overall polarizations of the BTO/STO superlattice are therefore given by  $\mathbf{P} = \mathbf{P}_{\text{BTO}}^S / (1 + \alpha \epsilon_{\text{BTO}} / \epsilon_{\text{STO}})$ , where  $\alpha = \ell_{\text{STO}} / \ell_{\text{BTO}}$ , and  $\mathbf{P}_{\text{BTO}}^S$  is the polarization of strained bulk BTO, and  $\epsilon_{\text{BTO}}$  and  $\epsilon_{\text{STO}}$  are the dielectric constants of strained bulk BTO and bulk STO, respectively. The *dielectric slab* model correctly captures the interface mediated electrostatic coupling and predicts a nearly uniform local polarization profile along [001] in BTO/STO superlattices, which were consistent with results obtained from the DFT calculations as shown in Fig. 14b.

The above design rule has also been applied onto other similar systems composed of a strong FE material and an incipient FE material with large dielectric constant, such as  $\text{KNbO}_3/\text{KTaO}_3$  (KNO/KTO)<sup>183–186</sup> and  $\text{PTO}/\text{STO}$ <sup>25,187</sup> superlattices. KNO is isostructural of BTO, and it adopts the tetragonal structure of  $P4mm$  symmetry with spontaneous polarization about  $35 \mu\text{C}/\text{cm}^2$  above  $488 \text{ K}$ <sup>74</sup>. At lower temperature, KNO adopts rhombohedral symmetry with polarization along [111]<sup>74</sup>. On the other hand,

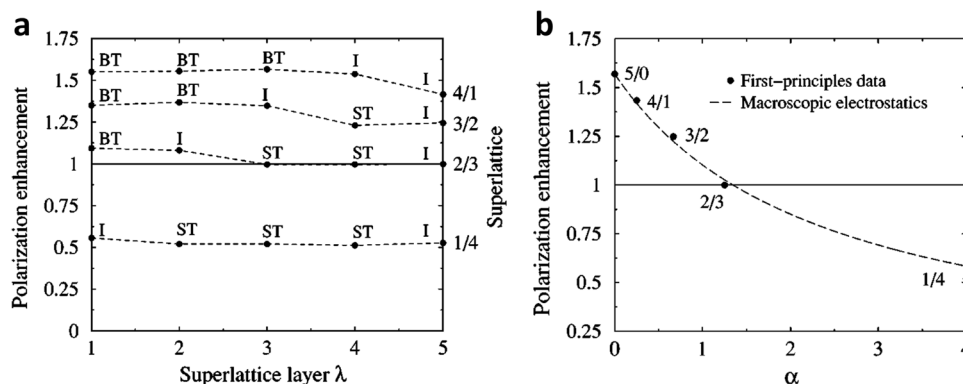


**Fig. 14** Electric polarization profiles in  $\text{BaTiO}_3/\text{SrTiO}_3$  superlattices. **a** Computed polarization enhancement ( $P_\lambda/P_0$ ) decomposition on each layer  $\lambda$  based on the Born effective charges and atomic displacements. **b** Overall enhancement as a function of  $\alpha = \ell_{\text{STO}}/\ell_{\text{BTO}}$  computed from first-principles calculations (filled circle) compared with that from dielectric slab model (dashed line). Reproduced with permission from ref. <sup>24</sup>. Copyright [2003] {AIP Publishing LLC}.

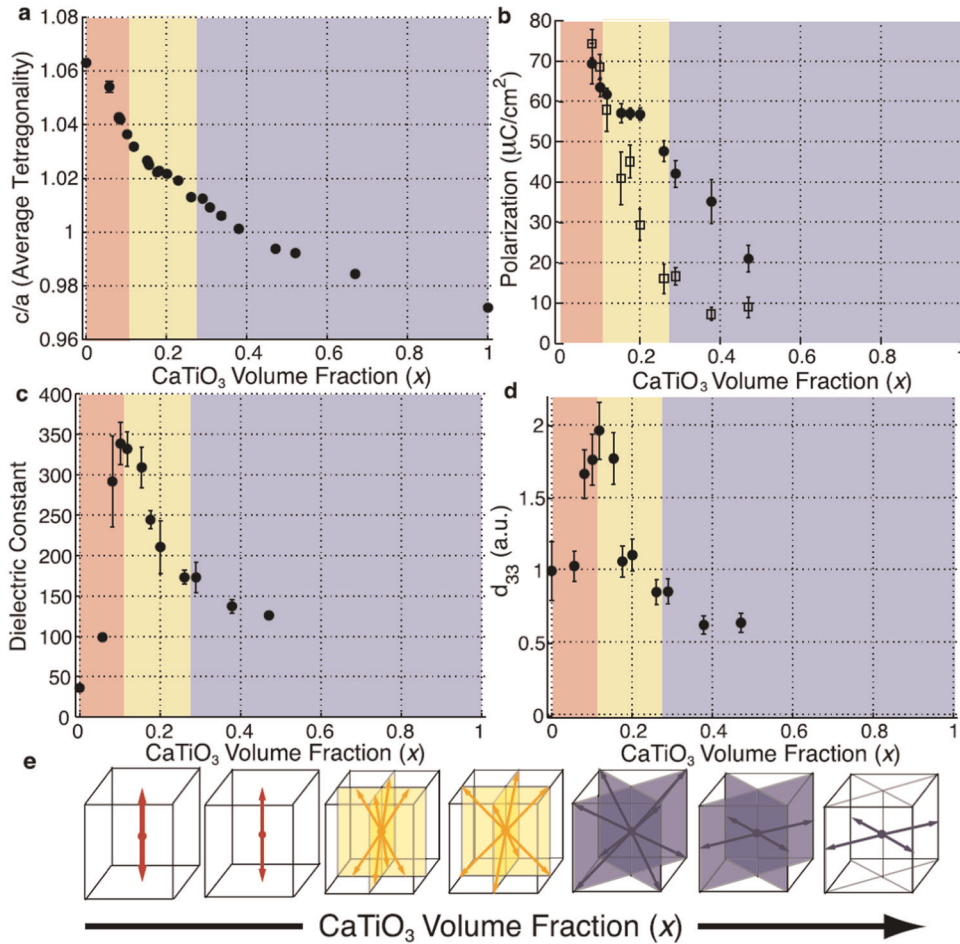


**Fig. 15** Ferroelectricity related properties in  $\text{PbTiO}_3/\text{CaTiO}_3$  superlattices. **a** Tetragonality, **b** polarization, **c** dielectric constant, **d** piezoelectric coefficient, and **e** evolution of polarization vector as a function of  $\text{CaTiO}_3$  volume fraction. Reproduced with permission from ref. <sup>191</sup>. Copyright [2012] {American Physical Society}.

KTO is also an incipient FE perovskite similar to STO. However, it does not develop an AFD transition but remains cubic at low temperature<sup>74,188</sup>. In artificial KNO/KTO superlattices grown on KTO substrate, a large out-of-plane polarization is found to be induced in the KTO layers, which is due to the electrostatic coupling effect through the interfaces as discussed. In addition, it was found that the compressive strain exerted by the KTO substrate is not sufficient enough to drive the KNO constituents from rhombohedral phase into tetragonal phase<sup>184,185</sup>. As a result, both out-of-plane and in-plane polarization components are found to be present in the KNO layers of the superlattice. The main difference between out-of-plane and in-plane polarization components is that the former varies continuously due to the fixed electric displacement field, while the latter allows abrupt changes through different layers. The design mechanism based on interface electrostatic coupling has also been successfully applied on the  $(\text{PTO})_n/(\text{STO})_3$  system, where PTO is a tetragonal FE material with strong polarization at room temperature and STO is an incipient FE material<sup>74,189</sup>. Similar to BTO/STO superlattice, out-of-plane polarization was found to be induced in the STO layers, and the local polarization profile can be well described by the *dielectric slab* model for  $n \geq 3$  when the interface atomic reconstruction can be neglected<sup>25,190</sup>.

In the bicolor artificial superlattice, if bulk polarization of one constituent perovskite is along [001] direction while the other is long [110] direction, polarization in the interfacial layers will be observed to rotate from out-of-plane gradually to the in-plane direction due to the electrostatic coupling effect. As an example,

Sinsheimer et al. fabricated artificial PTO/CTO superlattices on [001] surface of STO substrates using the off-axis radio frequency magnetron sputtering method<sup>191</sup>. For all superlattices fabricated, CTO thickness was fixed to be three layers, while the PTO thickness was varied. The tetragonality, FE, piezoelectric, and dielectric properties of PTO/CTO superlattices were measured as a function of the CTO volume fraction  $x = n_{\text{CTO}}/n_{\text{CTO}} + n_{\text{PTO}}$  as shown in Fig. 15, where  $n_{\text{CTO}}$  and  $n_{\text{PTO}}$  are number of CTO and PTO unit cells. It was observed that when  $x$  approaches to 0, polar properties of the superlattices are largely governed by the PTO layers in such a way that a large polarization along [001] direction is observed; for  $x$  closes to 1, the properties of superlattices are dominated by CTO constituents, and polarization along [110] direction is observed due to large tensile strain imposed by STO substrate as discussed in the section of "Ferroelectricity in thin films under epitaxial strain". However, for  $0 < x < 1$ , PTO/CTO superlattices develop a continuous polarization rotation from [001] to [110] as the thickness of PTO layers decreases, and their structures undergo consecutive phase transitions from  $\mathbf{T}-\mathbf{M}_C-\mathbf{M}_A-\mathbf{O}$  as shown in Fig. 15, where  $\mathbf{T}$  represents tetragonal phase with polarization direct to [001] axis,  $\mathbf{M}_C$  and  $\mathbf{M}_A$  denote two monoclinic phases with polarizations along  $[u0v]$  and  $[uuv]$  ( $u < v$ ) directions respectively, and  $\mathbf{O}$  stands for orthorhombic phase with polarization point to [110] direction. Such a polarization rotation due to the electrostatic coupling between PTO and CTO layers gives rise to highly tunable dielectric and piezoelectric properties. As a result, the out-of-plane piezoelectric constant  $d_{33}$

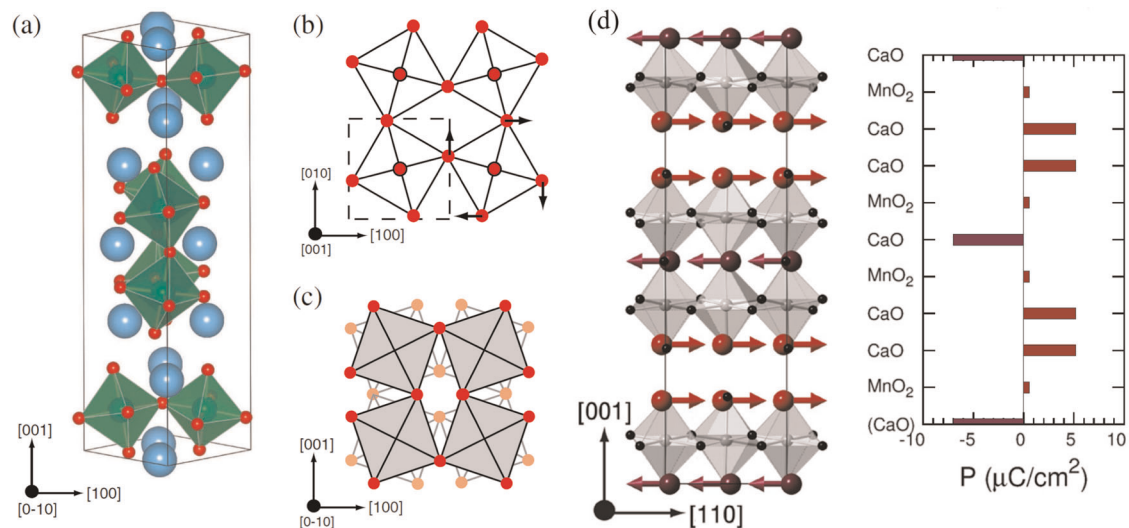


**Fig. 16** Crystal structure and structural distortions in hybrid improper ferroelectric materials of  $\text{Ca}_3\text{Mn}_2\text{O}_7$ . **a** Ball-and-stick model of ferroelectric ground state structure of  $\text{Ca}_3\text{Mn}_2\text{O}_7$  with  $A2_1am$  space group symmetry. **b** Structural distortion of oxygen octahedral rotation ( $X_2^+$  mode). **c** Structure distortion of oxygen octahedral tilt ( $X_3^-$  mode). **d** Layer decomposition of polarizations within the plane along [110] direction. Figure 16a–c are reproduced with permission from ref. <sup>170</sup>. Copyright [2011] {American Physical Society}. Figure **d** is reprinted from ref. <sup>200</sup>, Copyright (2012), with permission from Elsevier.

is greatly enhanced in the samples at the morphotropic phase boundary<sup>97,192</sup> of the **T–M<sub>C</sub>** transition.

#### Hybrid improper ferroelectricity

Based on the nature of structural instability that gives rise to the polar distortion, FE materials can be classified into the so-called *proper* and *improper* ones. In proper FE materials, such as PTO or BTO, the polar distortion originates directly from the unstable polar phonon mode at  $\Gamma$  point of the Brillouin zone, which is the primary order parameter according to the Landau second order phase transition theory<sup>104,193,194</sup>. The variation of energy with polar distortion around PE phase displays a characteristic of double-well shape in the proper FE, and the two energy minima with antiparallel polarization can be switched to each other through an external electric field without involving any other structural distortions. The microscopic origin of stabilizing force associated with proper FE distortion is closely related to the strong covalent bond or orbital hybridization between cation and anion<sup>193</sup>. On the other hand, the polar mode in improper FE materials is not intrinsically unstable, but only becomes unstable after the development of the primary structural distortion which is usually zone-boundary phonon mode<sup>160,195</sup>. For example, hexagonal  $\text{YMnO}_3$ <sup>196</sup> is a prototype of improper FE perovskite. Its polar mode is stable by itself in its centrosymmetric phase; it only becomes unstable after the development of zone-boundary mode with wave vector  $\mathbf{q} = (1/3, 1/3, 0)$ , which triples the unit cell size to accommodate the rotation of the  $\text{MnO}_5$  trigonal bipyramids and a buckling of the Y–O layers. The microscopic origin of improper FE can be related to the adjusted electrostatic interaction with the development of the primary structural distortion<sup>197</sup>. Therefore, improper FE is also named after *geometric* FE. When an external electric field is applied to switch the improper FE, the polar mode together with the primary order parameter should be switched simultaneously<sup>92</sup>.

Recently, the so-called hybrid improper FE has emerged as an important new subcategory of the improper FE materials. As characteristic of hybrid improper FE, the development of polar distortion involves at least two nonpolar modes with distinct symmetries<sup>170,198,199</sup>. The mechanism of hybrid improper FE has been demonstrated in the multiferroic  $\text{Ca}_3\text{Mn}_2\text{O}_7$ <sup>170</sup> belonging to the Ruddlesden–Popper family with a general formula of

$A_{n+1}B_nO_{3n+1}$ .  $\text{Ca}_3\text{Mn}_2\text{O}_7$  consists of  $\text{ABO}_3$  perovskite blocks stacking along [001] direction with an extra AO layer inserted every  $n$  ( $=2$ ) cells as shown in Fig. 16a. The lattice dynamics studies show that the polar distortion is stable in its centrosymmetric phase with  $I4/mmm$  symmetry. However, a polar structural distortion ( $\Gamma_5^-$  mode) emerges upon the distortions associated with oxygen rotation ( $X_2^+$  mode) and tilt ( $X_3^-$  mode) develop simultaneously as shown in Fig. 16b–d. As a result,  $\text{Ca}_3\text{Mn}_2\text{O}_7$  transforms into  $A2_1am$  FE phase. In addition, the energy landscape of the polar mode displays linear behavior after both oxygen octahedron rotation and tilt develop, which is consistent with the improper nature of FE through the symmetry allowed coupling term  $\sim Q_{X_2^+}Q_{X_3^-}Q_{\Gamma_5^-}$  that lowers the total energy in the FE phase, where  $Q$  denotes the mode amplitude.

In perovskite superlattices, oxygen octahedral rotations and tilts are common structural distortions, which provides rich opportunities to induce polarization via the hybrid improper FE mechanism. The interface induced FE through the hybrid improper FE mechanism was first discovered experimentally in PTO/STO superlattices by Dawber et al.<sup>25</sup>. In all 20 different superlattices under investigation, the thickness of STO layers was held fixed to be three cells, while the thickness of PTO layers was varied. According to the electrostatic coupling effect through interfaces as discussed in the section of “Electrostatic coupling effect via interfaces”, both the polarization and tetragonality of the superlattices are expected to be decreased as the PTO layer thickness decreases. A simple model was built,  $E(\mathbf{P}_p, \mathbf{P}_s) = xU_p(\mathbf{P}_p) + (1-x)U_s(\mathbf{P}_s) + E_{\text{elec}}(\mathbf{P}_p, \mathbf{P}_s)$ , in order to describe the FE in the superlattices by taking into account the electrostatic coupling effect through the interfaces. In the above,  $U_p(\mathbf{P}_p)$  and  $U_s(\mathbf{P}_s)$  represent the total energies of bulk PTO and STO as a function of their zero-field polarizations  $\mathbf{P}_p$  and  $\mathbf{P}_s$  which were obtained from DFT calculations,  $x = n_p/(n_p + n_s)$  is the PTO volume fraction and the last term is an electrostatic energy between the PTO and STO layers. As shown in Fig. 17a, this model agrees well with the DFT calculations when number of PTO layers ( $n_p$ ) exceeds that of STO layers ( $n_s$ ),  $n_p/n_s > 1$ . For  $n_p/n_s$  is less than 1, polarization predicted from the model vanishes, however, experimental measurement gave surprisingly nonzero polarization in those superlattices. In order to exclude the role of temperature effect in the unexpected recovery of FE, the total energies  $U_p(\mathbf{P}_p)$  and  $U_s(\mathbf{P}_s)$  in above electrostatic model were then replaced by the

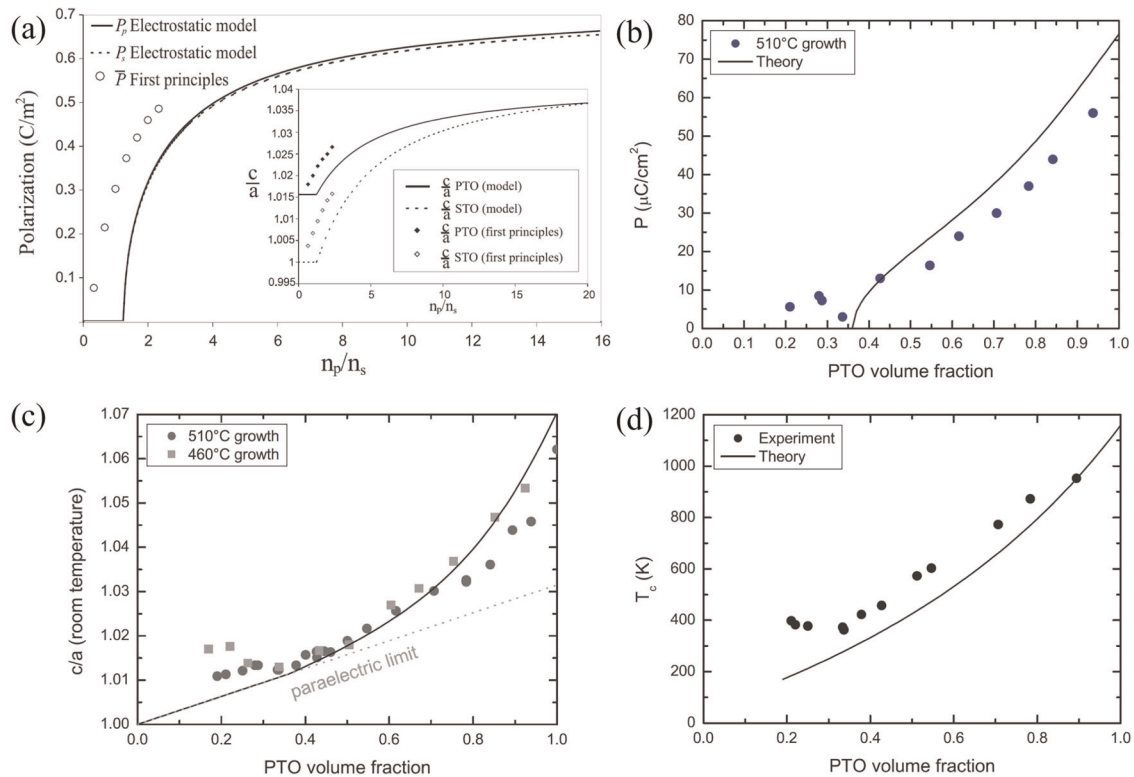


**Fig. 17 Polarization, tetragonality and ferroelectric phase transition temperature of PbTiO<sub>3</sub>/SrTiO<sub>3</sub> superlattices.** **a** Electric polarizations predicted by Landau–Devonshire phenomenological model and first-principles calculations as a function of the ratio between PbTiO<sub>3</sub> fraction and the SrTiO<sub>3</sub> fraction ( $n_p/n_s$ ) in the superlattices. **b** The measured and predicted electric polarizations as a function of PbTiO<sub>3</sub> volume fraction in the superlattices based on positive up negative down experiment and Landau–Devonshire phenomenological theory, respectively. **c** Tetragonality of two series of samples grown on 460 °C and 510 °C as a function of PbTiO<sub>3</sub> volume fraction in the superlattices. **d** Experimental (dots) and theoretical (solid lines) ferroelectric structural transition temperatures as a function of PbTiO<sub>3</sub> volume fraction in the superlattices. Reprinted with permission from ref. <sup>190</sup>. Copyright (2008) John Wiley & Sons, Inc.

Helmholtz free energies<sup>190</sup>. As shown in Fig. 17b–d, results from the revised model successfully predicted polarization, tetragonality and transition temperature for PTO/STO superlattices with  $n_p/n_s > 1$ , but still failed to reproduce the results in superlattices with low PTO volume fraction. Obviously, the failure of electrostatic coupling model in predicting FE of superlattices with ultra-thin PTO layer thicknesses indicates that electrostatic coupling alone is not sufficient, and some unexpected interface effect should take place here.

In order to elucidate the interfacial origin of the unusual FE behavior in PTO/STO superlattices, Bousquet et al.<sup>162</sup> carefully studied the structural distortions on the 1/1 superlattice based on DFT energy minimizations. The structural relaxation showed that 1PTO/1STO superlattice at ground state adopts a polar structure with  $P4bm$  symmetry. The polar structure can be considered as the combination of three distinct structural distortions added on the centrosymmetric reference structure with  $P4/mmm$  symmetry which are polar distortion ( $\Gamma_3^-$  mode), out-of-phase ( $M_4^-$  mode) and in-phase ( $M_2^+$  mode) octahedral rotations around [001] axis as shown in Fig. 18a–c, respectively. In order to study their relative importance in stabilizing the observed ground state, the three distortions have been systematically added onto the centrosymmetric reference structure. It was found that the polar structural distortion alone only has a relatively small energy gain as shown by the shallow FE double-well potential in Fig. 18d. Surprisingly, the FE ground state is further stabilized when both of the in-phase and out-of-phase oxygen octahedral rotations are allowed to develop, which seem to be contradictive to the conventional belief that the AFD and FE distortions are in strong competition in perovskites<sup>123</sup>. The following Landau free energy expansion the

symmetry analysis reveals that the FE is actually promoted when two types of AFD modes are present via the trilinear coupling terms  $Q_{\Gamma_3^-} Q_{M_4^-} Q_{M_2^+}$  that greatly lowers the total energy in 1PTO/1STO supercell.

Similar distortions as observed in 1PTO/1STO supercell were also clearly identified at the interfaces in PTO/STO superlattices of other thicknesses, such as superlattices with 3/3, 5/3, and 7/3 periods. The appearance of the octahedral rotations can be attributed to the intrinsic structural instabilities at Brillouin zone boundary points in both PTO and STO in their cubic phases<sup>104,114</sup>. As an incipient FE material, the bulk STO at ground state barely shows any FE polarization<sup>122</sup>, and has an octahedral rotation around the [001] axis. On the other hand, the appearance of the octahedral rotation in PTO is strongly dependent on the electric boundary condition. Hong and Vanderbilt<sup>95</sup> studied the complex energy landscape of STO and PTO perovskites as functions of varying applied electric displacement fields. It was found the AFD mode associated with the oxygen octahedral rotation in bulk PTO was absent in high electric displacement fields and recovered under at low electric displacement fields. A similar scenario occurs in PTO/STO superlattices when the STO portion is increased gradually in the experiment carried out by Bousquet et al.<sup>162</sup>.

A very similar effect induced by hybrid improper FE mechanism was also discovered at the interface of 1PTO/1PbZrO<sub>3</sub> short-period superlattice<sup>201</sup>. A careful inspection of the relaxed ground state of the above interface only superlattice revealed that an interesting pattern of structural distortions emerged, which are oxygen octahedral tilts around [110] axis ( $R_{110}$ ), and out-of-phase oxygen octahedral rotation around [001] axis ( $R_{001}$ ). In terms of Glazer notation, the above structural distortions are referred to as  $a^- a^- c^0$

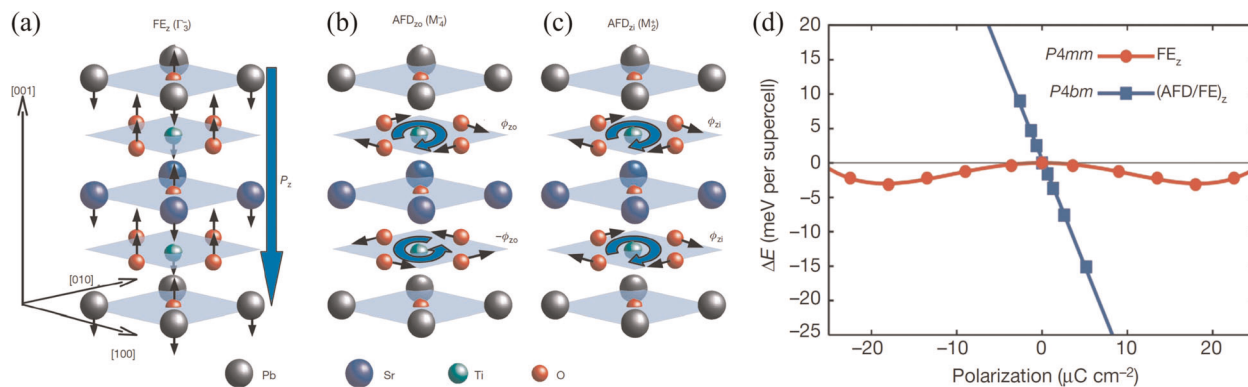


**Fig. 18 Schematic plots demonstrating the induced improper ferroelectricity in 1PbTiO<sub>3</sub>/15SrTiO<sub>3</sub> superlattice. a** Electric polarization along [001] direction is generated by zone center  $\Gamma_3^-$  mode. **b** Out-of-phase oxygen octahedral rotation is generated by zone boundary  $M_4^-$  mode. **c** In-phase oxygen octahedral rotation is generated by zone boundary  $M_2^+$  mode. **d** The calculated ground state total energies as a function of electric polarization by including  $\Gamma_3^-$  mode only, and  $\Gamma_3^-$  mode together with  $M_4^-$  and  $M_2^+$  all together. Figure 18a are reprinted with permission from ref. <sup>25</sup>, Copyright [2005] {American Physical Society}. Figure 18b–d are reprinted with permission from ref. <sup>162</sup>. Copyright (2008) Springer Nature.

and  $a^0a^0c^-$ , respectively<sup>202</sup>. Based on Landau-type energy expansion facilitated by group theory analysis, the interface structure actually promotes FE polarization along [001] ( $P_{001}$ ) and [110] axis ( $P_{110}$ ) which was enabled by a four-linear coupling term,  $\sim Q_{P001}Q_{P110}Q_{R001}Q_{R110}$  lowering the energy. If three of the four distortions are present, the fourth term which even was not unstable will be enhanced. Clearly, such induced FE belongs to improper FE in nature.

Beside the enhanced FE polarization in the FE/PE superlattice, the hybrid improper mechanism has also been applied onto inverse interface design of artificial FE materials from nonpolar perovskites only. As discussed above, the hybrid improper FE in Ruddlesden–Popper  $A_3B_2O_7$  materials (such as  $\text{Ca}_3\text{Mn}_2\text{O}_7$  or  $\text{Ca}_3\text{Ti}_2\text{O}_7$ ) can be understood to arise from the non-cancellation of antipolar displacements of A-site cations<sup>23,170,198</sup>. A similar antipolar displacement on A-site can be also found in many  $\text{ABO}_3$  perovskites of  $Pnma$  phase such as CTO, which is a common crystalline symmetry in perovskites. The  $Pnma$  structure is evolved from the reference cubic structure with  $Pm\bar{3}m$  symmetry via structural distortions including two distinct oxygen octahedral rotation patterns of  $a^0a^0c^+$  ( $Q_M$ ) and  $a^-a^-c^0$  ( $Q_R$ ), as shown in Fig. 19a, b, respectively. The antipolar distortion  $X_5^+$  ( $Q_X$ ) develops at ground of CTO, through a symmetry-allowed trilinear coupling free energy term  $\sim Q_M Q_R Q_X$  that largely lowers the energy<sup>28</sup>. Unlike the Ruddlesden–Popper systems, the oxygen octahedral connectivity is well preserved in  $Pnma$  structure, the octahedral rotations in bulk CTO cannot break the inversion symmetry. As a result, perovskite with  $Pnma$  symmetry yields an anti-polar ground state as shown in Fig. 19c. However, the above has been overcome by Fennie and Rondinelli recently<sup>26</sup>. They theoretically designed the  $1\text{ABO}_3/1\text{A}'\text{BO}_3$  supercell based on nonpolar  $Pnma$  perovskites, which can be also considered as artificial double perovskites with two chemically distinct A-site species<sup>26,200</sup>. The changes in the chemical environments allow the inversion symmetry breaking via the above improper FE mechanism. Similar to that in  $\text{Ca}_3\text{Mn}_2\text{O}_7$ , the antipolar displacements of two alternate AO layers along [001] direction no longer exactly equal to each other, leaving a nonzero residual overall polarization as shown in Fig. 19d. Since the inversion symmetry breaking originates from the non-cancellation of two distinct antipolar modes induced by two primary oxygen octahedral rotations, it is therefore classified as the hybrid improper mechanism<sup>20,200</sup>. Furthermore, it was found that if the magnitudes of octahedral rotations and tilts are comparable in bulk  $\text{ABO}_3$  and  $\text{A}'\text{BO}_3$  then the antipolar A-site displacement will be similar. As a result, the overall polarization is small due to nearly canceled antipolar modes of AO and A'O layer.

Therefore, it was proposed that a strong  $Pnma$  perovskite  $\text{ABO}_3$  of small Goldschmidt tolerance factor and a weak  $Pnma$  perovskite  $\text{A}'\text{BO}_3$  of large tolerance factor should be chosen in building the  $1\text{ABO}_3/1\text{A}'\text{BO}_3$  superlattice in order to achieve relatively large polarization. Due to the interface effect in nature, the total polarization is found to be maximized in the dense interface limit in  $1\text{ABO}_3/1\text{A}'\text{BO}_3$  systems<sup>20</sup>. In addition, the FE transition temperature is determined by the structural phase transition with oxygen octahedral rotations and tilts, which is usually well above room temperature for many perovskites with  $Pnma$  structure<sup>23,162,190</sup>. Therefore, the hybrid improper mechanism provides a promising way to design room temperature FE and multiferroic materials.

Following the above design rule,  $\text{ASnO}_3/\text{A}'\text{SnO}_3$  SLs (A, A' = Ca, Sr, and Ba) are typical examples of improper FEs successfully predicted by first-principles simulations<sup>203</sup>. Because of the large radius of Ba atom, neither octahedral rotation nor tilt occurs in the  $\text{BaSnO}_3$  layer. In contrast, the smaller sizes of A-site cations of Ca or Sr allow oxygen octahedral rotation and tilt to develop resulting in large antipolar structural distortion as represented by the in-plane A-site displacements in both  $\text{CaSnO}_3$  and  $\text{SrSnO}_3$  layers as previously described. As a result, FE polarizations of 10.379 and 2.778  $\mu\text{C}/\text{cm}^2$  are induced in both  $\text{BaSnO}_3/\text{CaSnO}_3$  and  $\text{BaSnO}_3/\text{SrSnO}_3$  superlattices. It should be noted that none of them is polar by itself in natural ground state. Not surprisingly,  $\text{BaSnO}_3/\text{CaSnO}_3$  has a larger polarization value than the latter due to the fact that  $\text{CaSnO}_3$  is a stronger  $Pnma$  perovskite than that of  $\text{SrSnO}_3$  as discussed. By the same token, the germanate based  $1\text{AGeO}_3/1\text{A}'\text{GeO}_3$  superlattice (A, A' = Mg, Ca, Sr, and Ba) and  $1\text{LaGaO}_3/1\text{YGaO}_3$  have been predicted to be FE at room temperature<sup>20</sup>. The hybrid improper FE mechanism has been also successfully applied onto  $Pnma$  perovskite with the B-site atom replaced by transition metal element with partially occupied  $d$  states in order to design novel multiferroic materials for desired magnetoelectric effect<sup>204,205</sup>.

Based on first-principles calculations, Ghosh et al.<sup>204</sup> have explored the structural and magnetic properties of the orthorhombic ferrite perovskite family of  $\text{LnFeO}_3$ , where Ln denotes a cation belonging to the lanthanide series or Yttrium. They found that  $1\text{LaFeO}_3/1\text{LnFeO}_3$  (Ln = Ce, Nd, Sm, Gd, Dy, Tm, Lu, and Y) supercells display both FE and FM properties at ground state. As expected, the FE polarization originates from the hybrid improper mechanism.  $\text{LnFeO}_3$  ( $\text{LaFeO}_3$ ) has a strong (weak) in-plane antipolar structural distortions due to the much smaller cation size of Ln than that of La. Therefore, a nonzero in-plane polarization is induced from 2.2  $\mu\text{C}/\text{cm}^2$  for Ln = Ce to

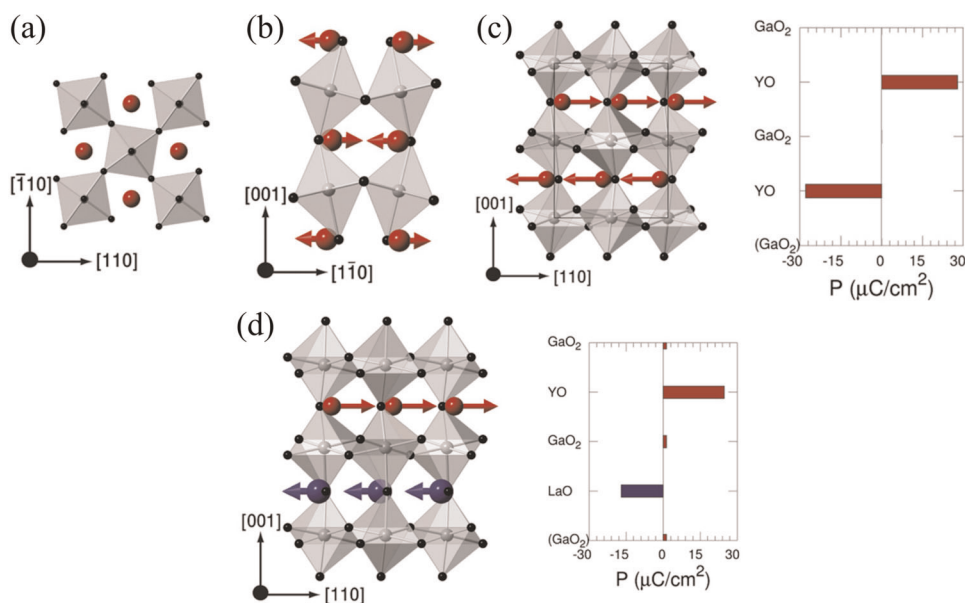


**Fig. 19** Illustration of the hybrid improper ferroelectricity in artificial perovskite superlattices. **a** Oxygen octahedral rotation around [001] direction. **b** Oxygen octahedral tilt around [110] direction. **c** Antipolar displacement ( $X_5^+$  mode) on A-site atoms. **d** Residual polarization arises from the non-canceled antipolar A-site displacements in  $1\text{LaGaO}_3/1\text{YGaO}_3$  superlattice. Reprinted from ref. <sup>200</sup>, Copyright (2012), with permission from Elsevier.

$11.6 \mu\text{C}/\text{cm}^2$  for  $\text{Ln} = \text{Lu}$ , at the interfaces of the  $1\text{LaFeO}_3/1\text{LnFeO}_3$  superlattices due to the difference between the above two antipolar modes<sup>204</sup>. Surprisingly, the oxygen octahedral rotation and tilt can induce weak ferromagnetism due to the canted spins in G-AFM ordering of Fe atoms. Such canting arises from the Dzyaloshinskii–Moriya (DM)<sup>206,207</sup> exchange interactions between Fe spins. Moreover, DFT calculations suggested that these superlattices display a linear magnetoelectric effect larger than that observed in the prototypical magnetoelectric materials such as  $\text{Cr}_2\text{O}_3$  and  $\text{BiFeO}_3$ . Based on the superexchange energies from first-principles calculations and mean-field theory, the magnetic transition temperature of  $1\text{LaFeO}_3/1\text{YFeO}_3$  was estimated to be close to the Néel temperature  $\text{LaFeO}_3$  as high as  $\sim 740$  K.

In addition, the hybrid improper mechanism was also successfully applied onto the inverse interface design of double perovskite superlattices. Similar to the  $Pnma$  phase perovskite, the double perovskite oxide can also adopt complex structural distortions combining oxygen octahedral rotation and tilt, adopting the  $a^-a^-c^+$  Glazer tilt pattern. As a result, the antipolar distortion similar to that in  $Pnma$  perovskite occurs in double perovskite oxides such as  $R_2\text{NiMnO}_6$ , which are FM insulators ( $R$  is a rare earth element), as shown in Fig. 20a<sup>208,209</sup>. Zhao et al. have theoretically investigated the hybrid improper FE in  $R_2\text{NiMnO}_6/\text{La}_2\text{NiMnO}_6$  short period superlattices<sup>210</sup>. It was found that a spontaneous polarization is induced due to the different magnitudes of displacements between  $R$  and La associated with the antipolar displacement. Similar to that for perovskite  $1\text{ABO}_3/1\text{A}'\text{BO}_3$  superlattices, the interface induced polarization in  $R_2\text{NiMnO}_6/\text{La}_2\text{NiMnO}_6$  increases as the ionic radius of rare-earth  $R$  decreases as shown in Fig. 20b. This is due to the enhancement of oxygen octahedral rotation and tilt in  $R_2\text{NiMnO}_6$  through the trilinear coupling term. The polarization ranges from 1.4 to  $9.2 \mu\text{C}/\text{cm}^2$  for  $R = \text{Ce}, \text{Pr}, \text{Nd}, \text{Sm}, \text{Gd}, \text{Tb}, \text{Dy}, \text{Ho},$  and  $\text{Er}$ . In particular, for  $\text{Ce}_2\text{NiMnO}_6/\text{La}_2\text{NiMnO}_6$  short period superlattices, the combined DFT and Monte Carlo simulations predicted the Curie temperature to be 290 K as shown in Fig. 20c, which makes it a candidate of room temperature FE and FM materials.

#### Interfacial reconstructions of structural instabilities

As far as the structural distortion is concerned, only a few perovskites are dominated by polar mode, such as BTO, PTO, and KNO in its natural ground state. More complex structural distortions associated with the oxygen octahedral rotation and tilt usually occur<sup>27,164–166,168</sup>. The idealized cubic structure of perovskites can develop up to 15 distinct Glazer rotation patterns in total<sup>28,169,211</sup>. The most common oxygen octahedral rotation patterns occur in the  $Pnma$  space group symmetry, such as CTO. The  $R3c$  symmetry, such as  $\text{BiFeO}_3$  and  $\text{LiNbO}_3$ , is relatively less commonly seen in perovskites. The oxygen octahedral rotation pattern in  $Pnma$  perovskite can be depicted as the in-phase oxygen octahedral rotation around [001] axis and the oxygen octahedral tilt around [110] ( $a^-a^-c^+$  in Glazer notation), which originate from the structural instabilities at  $M$  and  $R$  points of Brillouin zone, respectively. As we have discussed earlier in the section of “Tunable band gap under epitaxial strain”, the antipolar distortion  $X_5^+$  mode is strongly favored in  $Pnma$  perovskite due to the trilinear coupling mechanism, resulting in its paraelectric ground state. On the other hand, the oxygen octahedral rotation pattern in  $R3c$  can be described as the out-of-phase oxygen octahedral rotation around [001] axis combined with oxygen octahedral tilt around [110] axis ( $a^-a^-a^-$  in Glazer notation), both of which originated from the  $R$  point instabilities in the Brillouin zone. The  $R3c$  perovskite is compatible with a large FE polarization. For example, the spontaneous polarization in  $\text{BiFeO}_3$ <sup>212</sup> and  $\text{LiNbO}_3$ <sup>213</sup> are found to be  $88.7$  and  $71 \mu\text{C}/\text{cm}^2$ , respectively. In particular, BFO is one of most studied room temperature multiferroic materials, in which the weak FM due to spin canting was recently confirmed in experiments<sup>212,214</sup>. Unfortunately, compared to the widely spread  $Pnma$  perovskites, the perovskites with  $R3c$  symmetry are rarely seen<sup>8,28,167</sup>.

However, recent theoretical studies suggested that, for many  $Pnma$  perovskites, the  $R3c$  structure is actually one of the low-lying metastable states<sup>215</sup>. The energetics between its ground state with  $Pnma$  structure and metastable  $R3c$  structures have been systematically studied by Wang et al.<sup>8</sup> recently by using CTO as the prototypical perovskite. In their work, they have proposed effective Hamiltonian models to describe the energy for ground state  $Pnma$  as well as metastable  $R3c$  phase of CTO, which was

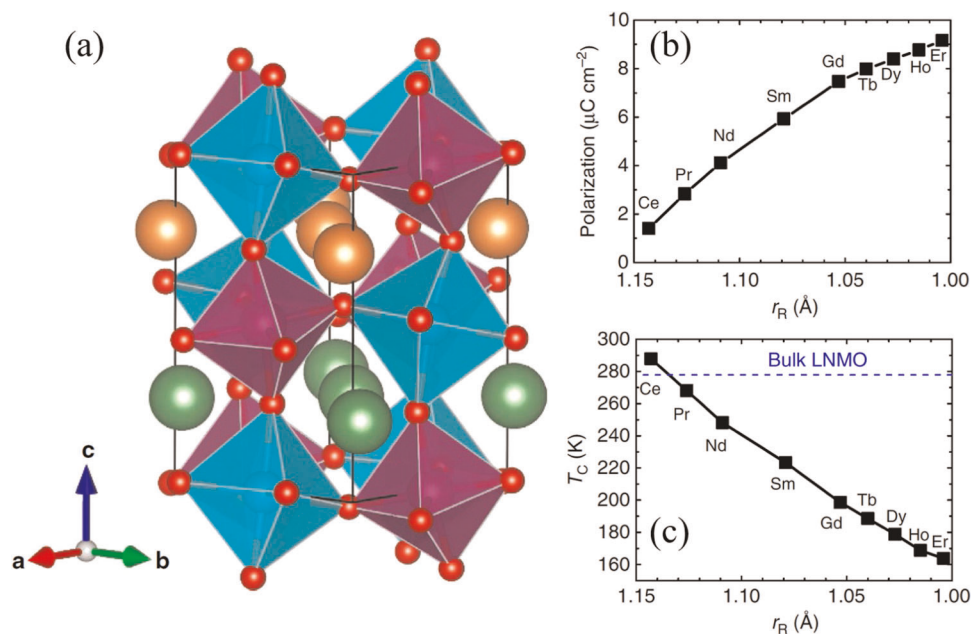


**Fig. 20** Crystal structure, electric polarizations, and magnetic phase transition temperatures of  $R_2\text{NiMnO}_6/\text{La}_2\text{NiMnO}_6$  ( $R$ : rare earth element) superlattices. **a** The ball-and-stick model of  $R_2\text{NiMnO}_6/\text{La}_2\text{NiMnO}_6$  superlattices; the  $\text{La}^{3+}$ ,  $R^{3+}$ ,  $\text{Ni}^{2+}$ ,  $\text{Mn}^{4+}$ , and  $\text{O}^{2-}$  ions are displayed as green, orange, cyan, purple, and red spheres, respectively. **b** The theoretical electric polarization, and **c** the predicted Curie temperatures as a function of the rare-earth ionic radius. Reprinted with permission from ref. <sup>210</sup>. Copyright (2014) Springer Nature.

assumed to be coherently grown on the STO substrate. The effective Hamiltonian was built from the PE high-symmetry reference structure ( $P4/mmm$ ) and the energies due to structural distortions in term of irreducible representations were considered by the Laudau type coupling terms facilitated by space group theory. All the coupling constants in the energy expansions were numerically fitted based on the inputs of DFT total energies with various frozen structural distortions. As expected, the ground state  $Pnma$  structure of CTO is found to be favored by a large trilinear coupling term (including in-phase octahedron rotation around [001], octahedron tilt around [110], and in-plane anti-polar mode) that significantly lower the total energy, which results in the antipolar mode with large A-site atom displacement. On the other hand, the  $R3c$  phase of CTO is promoted by a four-linear coupling term (including in-plane and out-of-plane FE modes, out-of-phase octahedron rotation around [001], and octahedron tilt around [110]), which largely lowers the total energy. Compared to the PE  $Pnma$  CTO, the  $R3c$  CTO has a slightly higher energy 0.211 eV/cell (contains 20 atoms) than the former. Wang et al.<sup>8</sup> further derived the enthalpy functions of  $Pnma$  and  $R3c$  phases of CTO respectively by assuming that the oxygen octahedron rotation and tilt angles are adjustable parameters under experimental conditions. Very interestingly, they found that the  $R3c$  structure of CTO becomes energetically more stable than the  $Pnma$  phase if the angles of octahedron rotation and, in particular, the octahedron tilt are significantly reduced.

The result by Wang et al.<sup>8</sup> suggests that the functional  $R3c$  structure may actually be stabilized for many perovskites, which naturally exists as  $Pnma$  phase. However, the significant reduction in the oxygen octahedral rotation and tilt could not be easily achieved by the applied epitaxial strain. This is because the oxygen octahedral rotation and tilt angles are found to be only weakly tunable under mismatch strain<sup>175</sup>. On the other hand, the oxygen distortions are found to be highly dependent on chemical pressure which can be adjusted by the ionic radius, chemical bonding, and electronegativity<sup>169</sup>. As a matter of fact, the amplitudes of the oxygen octahedral rotation and tilt are sensitively dependent on the ionic radii of the cations in  $\text{ABO}_3$  perovskite. The above dependence can be quantified by the so-

called Goldschmidt tolerance factor  $t = (r_A + r_O)/\sqrt{2}(r_B + r_O)$ , in which  $r_A$ ,  $r_B$ , and  $r_O$  are ionic radii of A-site cation, B-site cation, and oxygen anion for a particular  $\text{ABO}_3$  material, respectively<sup>216</sup>. When  $t = 1$ , perovskites tend to retain high-symmetry structure without any distortions. When  $t > 1$ , A site ionic radii are much larger compare with B site, large A–O repulsive forces resist octahedral rotation and favor FE distortion with B site ions moving off center<sup>20,28,217</sup>. For  $t < 1$ , A site ionic radii are relatively small, under which the perovskites tend to develop large octahedral rotation and tilt<sup>20,28,217</sup>. In perovskite superlattices, the proximity effect has recently been identified in both theory<sup>102,117,218</sup> and experiments<sup>8</sup>. It was found that for one  $\text{ABO}_3$  with a small tolerance factor, its oxygen rotation and tilt will be significantly suppressed at the interfaces close to the second perovskite component with a relatively large tolerance factor.

Guided by the above mechanism, the stabilization of the  $R3c$  phase of CTO has been successfully realized at the interface of BTO/CTO superlattice through combined first-principles calculations and transmission electron microscopy by Wang et al.<sup>8</sup>. BTO is a perovskite with larger tolerance factor, which is strongly resistant to oxygen rotation and tilt at room temperature. Wang and co-workers investigated a number of  $n\text{BTO}/n\text{CTO}$  superlattices ( $n = 1 \dots 6$ ). In particular, the structural distortions of 6BTO/6CTO was analyzed in detail as shown in Fig. 21. The perovskite component far away from the interfaces can be described by the bulk properties. In the BTO region in the superlattice, the structural distortion is mainly contributed by the polar distortion along [001] direction, which is consistent with the FE phase of BTO with tetragonal structure at room temperature. Whereas in the CTO region of the superlattice, the structure distortions are dominated by large in-phase oxygen octahedral rotation around [001] axis and tilt around [110] axis. As already described in the section of “Hybrid improper ferroelectricity”, this particular  $Pnma$  structure results in large antipolar mode as shown by the clear zigzag type A-site atom displacement which points to opposite direction for alternative layers along [110] direction. However, the oxygen distortion pattern undergoes a significant reconstruction at the interfacial layers. As a result, the oxygen octahedral in two alternating layers of CTO at the interface were surprisingly found

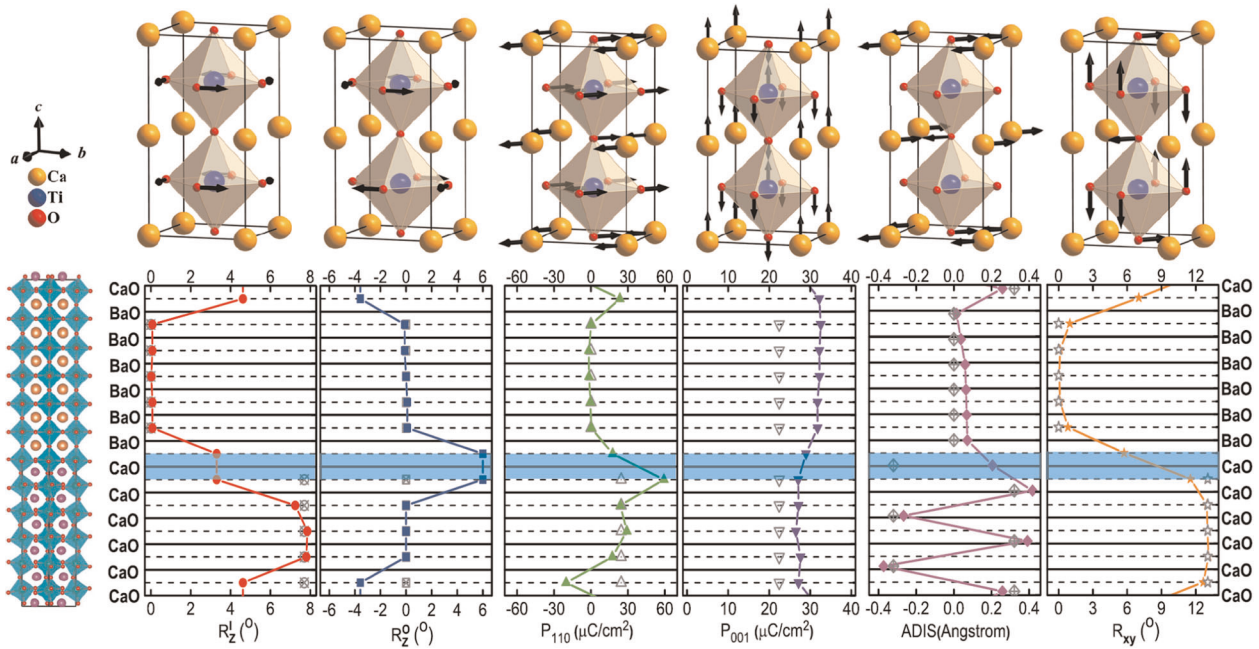


**Fig. 21** Layer by layer decomposed structural distortions and polarization in  $6\text{BaTiO}_3/6\text{CaTiO}_3$  superlattice.  $R_z^I$ ,  $R_z^O$  denote the in-phase and out-of-phase oxygen octahedral rotation around [001] direction respectively.  $P_{110}$ ,  $P_{001}$  represent the layer-by-layer decomposed polarization along [110] and [001] direction respectively. ADIS shows the atomic displacement of the A-site cations.  $R_{xy}$  describes the oxygen octahedral tilt around [110] direction. Reproduced with permission from ref. <sup>8</sup>. Copyright [2016] {American Physical Society}.

to be out-of-phase, which are due to the largely suppressed oxygen rotation and tilt angles by the proximity effect. The new pattern of oxygen rotation and tilt is exactly the same as the  $R3c$  structure as predicted by the enthalpy function in the above paragraph. The enhanced FE was evidenced by the calculated larger polarizations  $29.0 \mu\text{C}/\text{cm}^2$  than the values predicted by the electrostatic coupling model  $22.4 \mu\text{C}/\text{cm}^2$  in the section of "Multiferroic properties under epitaxial strain via spin-phonon coupling", which clearly indicates the interface enhanced FE.

Since the stabilization of the  $R3c$  structure takes place at the interfacial CTO layers, the enhanced polarization will depend on the density of the interfaces. As expected, the largest enhancement of polarization occurs in the 2BTO/2CTO supercell where the interface density is the maximum because the out-of-phase oxygen octahedral rotation requires a minimum number of two CTO layers. As the interface density decreases, the FE property is gradually dominated by the electrostatic coupling effect as we have discussed in the section of "Hybrid improper ferroelectricity". The above theoretical prediction is consistent with the more recent experiments performed on the BTO/CTO superlattices<sup>219,220</sup>. Jo et al. observed that the piezoelectric coefficient  $d_{33}$  of 2BTO/4CTO is measured to be  $54 \text{ pm}/\text{V}$  as large as the piezoelectric response in bulk BTO at room temperature. It is established that the piezoelectric tensor is proportional to the remnant polarization  $\mathbf{P}$  by  $d_{ij} = q_{ijk}P_k/\epsilon_{kj}$ ,<sup>221</sup> in which the  $d_{ij}$ ,  $q_{ijk}$ ,  $P_j$ , and  $\epsilon_{kj}$  represent piezoelectric coefficient, electrostrictive coefficient, remnant polarization and elastic constant respectively. Considering the fact that 60% of the 2BTO/4CTO superlattice are composed of nonpolar CTO layers, the above experiment implies a significantly larger FE polarization than the conventional estimation based on the electrostatic coupling effect only. However, considering the above described interface effect, it is easier to understand this phenomenon. The oxygen octahedral network will be reconstructed to form  $R3c$ -like structure resulting in the enhanced FE as well as piezoelectricity.

Such a interface design mechanism has been applied onto other superlattices as well, such as  $2\text{BaTiO}_3/2\text{CdTiO}_3$ ,  $2\text{KNbO}_3/2\text{NaNbO}_3$ , and  $2\text{KNbO}_3/2\text{AgNbO}_3$ . In general, the DFT calculations

show that the FE is enhanced by about 50–90%. Furthermore, based on first-principles calculations, Wang et al.<sup>8</sup> have proposed that the above interface mechanism can be even used to induce large FE polarization in artificial perovskite superlattices which are built from non-polar perovskites only. For the proposed  $1\text{A}'\text{BO}_3/1\text{A}''\text{BO}_3$  superlattice,  $\text{A}'\text{BO}_3$  is chosen to be strong  $Pnma$  structure with large in-phase rotation and tilt of oxygen octahedral, which is non-polar at ground state; on the other hand,  $\text{A}''\text{BO}_3$  is a strong "cubic" like perovskite with tolerance factor ( $t \sim 1$ ), so that neither the polar distortion or nor the oxygen octahedral rotation and tilt develop in  $\text{A}''\text{BO}_3$ . In the resulting  $1\text{A}'\text{BO}_3/1\text{A}''\text{BO}_3$  superlattices, the oxygen octahedral rotation and tilt are found to be suppressed in  $\text{A}'\text{BO}_3$  but are induced in  $\text{A}''\text{BO}_3$  perovskite. Most interestingly, the resulting oxygen octahedral network at ground state exhibits out-of-phase octahedral rotation with octahedral tilt, which is exactly described by the  $R3c$  structure. Concomitantly, large polar distortions along [110] and [001] direction develop in all the proposed materials such as  $1\text{CdSnO}_3/1\text{BaSnO}_3$ ,  $1\text{CdHfO}_3/1\text{BaHfO}_3$ , and  $1\text{CaZrO}_3/1\text{BaZrO}_3$ . In the above proposed superlattices, the in-plane polarization is found to be roughly  $\sqrt{2}$  times the out-of-plane component of polarization. This is exactly what one expects for the FE materials with  $R3c$  symmetry such as  $\text{BiFeO}_3$ . Because the prevalent  $Pnma$  structure in perovskite materials, this interface design mechanism introduces a new approach of designing novel functional materials. For example, if the FE could be recovered in orthogonal  $R\text{FeO}_3$ ,<sup>222–225</sup> ( $R = \text{Y, Gd, Tb, Dy, Ho, Er, Tm, Yb, Lu}$ ), the synthesis of room temperature multiferroic materials could be achieved.

## PERSPECTIVES

In conclusion, we have reviewed the recent progress in the design mechanisms in order to achieve functional properties in perovskite based thin-films and superlattices. In the article, we have focused on the ferroelectricity and multiferroic, which are highly sensitive to the presence as well as the nature of the interfaces grown in the superlattices. Furthermore, the observed enhanced functionalities also represent a delicate balance

between the long-range Coulombic interaction and short-range repulsion force or the competition among various magnetic orderings via the exchange interactions, which is further highly dependent on the particular mechanical and electric boundary conditions applied on the system. The modern thin-film technique provides an ideal playground to insert the designated interfaces in the superlattice by coherent epitaxial growth; at the same time, it can also implement the appropriate mechanical and electric boundary conditions through the choices of substrate and particular considerations in device fabrications. Over the last two decades, the first-principles calculations based on density functional theory have played a key role in conceiving the design rules of novel thin-film and superlattice as we have briefly reviewed. We have stressed that the comprehensive and proper treatments of mechanical and electric boundary conditions in theory are of crucial importance in validating those proposed design mechanisms.

Received: 18 December 2019; Accepted: 31 March 2020;

Published online: 08 May 2020

## REFERENCES

- Lee, H. N., Christen, H. M., Chisholm, M. F., Rouleau, C. M. & Lowndes, D. H. Strong polarization enhancement in asymmetric three-component ferroelectric superlattices. *Nature* **433**, 395–399 (2005).
- Ohtomo, A. & Hwang, H. Y. A high-mobility electron gas at the  $\text{LaAlO}_3/\text{SrTiO}_3$  heterointerface. *Nature* **427**, 423 (2004).
- Mundy, J. A. et al. Atomically engineered ferroic layers yield a room-temperature magnetoelectric multiferroic. *Nature* **537**, 523 (2016).
- Lee, D. et al. Emergence of room-temperature ferroelectricity at reduced dimensions. *Science* **349**, 1314–1317 (2015).
- Ismail-Beigi, S., Walker, F. J., Disa, A. S., Rabe, K. M. & Ahn, C. H. Picoscale materials engineering. *Nat. Rev. Mater.* **2**, 17060 (2017).
- Mannhart, J. & Schlom, D. G. Oxide interfaces—an opportunity for electronics. *Science* **327**, 1607–1611 (2010).
- Lee, J. H. et al. A strong ferroelectric ferromagnet created by means of spin–lattice coupling. *Nature* **466**, 954 (2010).
- Wang, H. et al. Stabilization of highly polar  $\text{BiFeO}_3$ -like structure: a new interface design route for enhanced ferroelectricity in artificial perovskite superlattices. *Phys. Rev. X* **6**, 011027 (2016).
- Dawber, M., Rabe, K. & Scott, J. Physics of thin-film ferroelectric oxides. *Rev. Mod. Phys.* **77**, 1083 (2005).
- Eason, R. *Pulsed Laser Deposition of Thin Films: Applications-Led Growth of Functional Materials*. (John Wiley & Sons, 2007).
- Panish, M. B. Molecular beam epitaxy. *Science* **208**, 916–922 (1980).
- Scott, J. F. Applications of modern ferroelectrics. *science* **315**, 954–959 (2007).
- Sai, N., Meyer, B. & Vanderbilt, D. Compositional inversion symmetry breaking in ferroelectric perovskites. *Phys. Rev. Lett.* **84**, 5636 (2000).
- Fennie, C. J. & Rabe, K. M. Magnetically induced phonon anisotropy in  $\text{ZnCr}_2\text{O}_4$  from first principles. *Phys. Rev. Lett.* **96**, 205505 (2006).
- Lee, J. H. & Rabe, K. M. Epitaxial-strain-induced multiferroicity in  $\text{SrMnO}_3$  from first principles. *Phys. Rev. Lett.* **104**, 207204 (2010).
- Lee, J. H. & Rabe, K. M. Coupled magnetic-ferroelectric metal-insulator transition in epitaxially strained  $\text{SrCoO}_3$  from first principles. *Phys. Rev. Lett.* **107**, 067601 (2011).
- Fennie, C. J. & Rabe, K. M. Magnetic and electric phase control in epitaxial  $\text{EuTiO}_3$  from first principles. *Phys. Rev. Lett.* **97**, 267602 (2006).
- Berger, R. F., Fennie, C. J. & Neaton, J. B. Band gap and edge engineering via ferroic distortion and anisotropic strain: the case of  $\text{SrTiO}_3$ . *Phys. Rev. Lett.* **107**, 146804 (2011).
- Wu, X., Stengel, M., Rabe, K. M. & Vanderbilt, D. Predicting polarization and nonlinear dielectric response of arbitrary perovskite superlattice sequences. *Phys. Rev. Lett.* **101**, 087601 (2008).
- Mulder, A. T., Benedek, N. A., Rondinelli, J. M. & Fennie, C. J. Turning  $\text{ABO}_3$  antiferroelectrics into ferroelectrics: design rules for practical rotation-driven ferroelectricity in double perovskites and  $\text{A}_3\text{B}_2\text{O}_7$  Ruddlesden-Popper compounds. *Adv. Funct. Mater.* **23**, 4810–4820 (2013).
- Sawada, K. & Nagaosa, N. Optical magnetoelectric effect in multiferroic materials: evidence for a Lorentz force acting on a ray of light. *Phys. Rev. Lett.* **95**, 237402 (2005).
- Warusawithana, M. P., Colla, E. V., Eckstein, J. & Weissman, M. Artificial dielectric superlattices with broken inversion symmetry. *Phys. Rev. Lett.* **90**, 036802 (2003).
- Oh, Y. S., Luo, X., Huang, F.-T., Wang, Y. & Cheong, S.-W. Experimental demonstration of hybrid improper ferroelectricity and the presence of abundant charged walls in  $(\text{Ca}, \text{Sr})_3\text{Ti}_2\text{O}_7$  crystals. *Nat. Mater.* **14**, 407 (2015).
- Neaton, J. B. & Rabe, K. M. Theory of polarization enhancement in epitaxial  $\text{BaTiO}_3/\text{SrTiO}_3$  superlattices. *Appl. Phys. Lett.* **82**, 1586–1588 (2003).
- Dawber, M. et al. Unusual behavior of the ferroelectric polarization in  $\text{PbTiO}_3/\text{SrTiO}_3$  superlattices. *Phys. Rev. Lett.* **95**, 177601 (2005).
- Rondinelli, J. M. & Fennie, C. J. Octahedral rotation-induced ferroelectricity in cation ordered perovskites. *Adv. Mater.* **24**, 1961–1968 (2012).
- Rondinelli, J. M., May, S. J. & Freeland, J. W. Control of octahedral connectivity in perovskite oxide heterostructures: an emerging route to multifunctional materials discovery. *MRS Bull.* **37**, 261–270 (2012).
- Benedek, N. A. & Fennie, C. J. Why are there so few perovskite ferroelectrics? *J. Phys. Chem. C* **117**, 13339–13349 (2013).
- Jones, R. O. Density functional theory: its origins, rise to prominence, and future. *Rev. Mod. Phys.* **87**, 897 (2015).
- Perdew, J. P. & Wang, Y. Accurate and simple analytic representation of the electron-gas correlation energy. *Phys. Rev. B* **45**, 13244 (1992).
- Perdew, J. P. & Zunger, A. Self-interaction correction to density-functional approximations for many-electron systems. *Phys. Rev. B* **23**, 5048 (1981).
- Perdew, J. P., Burke, K. & Ernzerhof, M. Generalized gradient approximation made simple. *Phys. Rev. Lett.* **77**, 3865 (1996).
- Zhang, Y., Sun, J., Perdew, J. P. & Wu, X. Comparative first-principles studies of prototypical ferroelectric materials by LDA, GGA, and SCAN meta-GGA. *Phys. Rev. B* **96**, 035143 (2017).
- Sun, J. et al. Accurate first-principles structures and energies of diversely bonded systems from an efficient density functional. *Nat. Chem.* **8**, 831 (2016).
- Sun, J., Ruzsinszky, A. & Perdew, J. P. Strongly constrained and appropriately normed semilocal density functional. *Phys. Rev. Lett.* **115**, 036402 (2015).
- Jia, F. et al. Cubic and tetragonal perovskites from the random phase approximation. *Phys. Rev. Mater.* **3**, 103801, (2019).
- Baroni, S., De Gironcoli, S., Dal Corso, A. & Giannozzi, P. Phonons and related crystal properties from density-functional perturbation theory. *Rev. Mod. Phys.* **73**, 515 (2001).
- Gonze, X. Adiabatic density-functional perturbation theory. *Phys. Rev. A* **52**, 1096 (1995).
- Hamann, D. R., Wu, X., Rabe, K. M. & Vanderbilt, D. Metric tensor formulation of strain in density-functional perturbation theory. *Phys. Rev. B* **71**, 035117 (2005).
- Wu, X., Vanderbilt, D. & Hamann, D. R. Systematic treatment of displacements, strains, and electric fields in density-functional perturbation theory. *Phys. Rev. B* **72**, 035105 (2005).
- Schlom, D. G. et al. Strain tuning of ferroelectric thin films. *Annu. Rev. Mater. Res.* **37**, 589–626 (2007).
- Lee, J. H. & Rabe, K. M. Large spin-phonon coupling and magnetically induced phonon anisotropy in  $\text{SrMO}_3$  perovskites ( $M = \text{V}, \text{Cr}, \text{Mn}, \text{Fe}, \text{Co}$ ). *Phys. Rev. B* **84**, 104440 (2011).
- Wang, H., He, L., Jiang, H., Steele, C. & Wu, X. Electronic origin of the spin-phonon coupling effect in transition-metal perovskites. *Phys. Rev. B* **96**, 075121 (2017).
- Stengel, M., Spaldin, N. A. & Vanderbilt, D. Electric displacement as the fundamental variable in electronic-structure calculations. *Nat. Phys.* **5**, 304–308 (2009).
- Stengel, M., Vanderbilt, D. & Spaldin, N. A. Enhancement of ferroelectricity at metal–oxide interfaces. *Nat. Mater.* **8**, 392–397 (2009).
- Junquera, J. & Ghosez, P. First-principles study of ferroelectric oxide epitaxial thin films and superlattices: role of the mechanical and electrical boundary conditions. *J. Comput. Theor. Nanosci.* **5**, 2071–2088 (2008).
- Beach, R. S. et al. Enhanced Curie temperatures and magnetoelastic domains in  $\text{Dy/Lu}$  superlattices and films. *Phys. Rev. Lett.* **70**, 3502 (1993).
- Gan, Q., Rao, R. A., Eom, C. B., Garrett, J. L. & Lee, M. Direct measurement of strain effects on magnetic and electrical properties of epitaxial  $\text{SrRuO}_3$  thin films. *Appl. Phys. Lett.* **72**, 978–980 (1998).
- Sato, H. & Naito, M. Increase in the superconducting transition temperature by anisotropic strain effect in  $(001) \text{La}_{1.85}\text{Sr}_{0.15}\text{CuO}_4$  thin films on  $\text{LaSrAlO}_4$  substrates. *Phys. C* **274**, 221–226 (1997).
- Bozovic, I., Logvenov, G., Belca, I., Narimbetov, B. & Sveklo, I. Epitaxial strain and superconductivity in  $\text{La}_{2-x}\text{Sr}_x\text{CuO}_4$  thin films. *Phys. Rev. Lett.* **89**, 107001 (2002).
- Huang, L., Wu, F. & Li, J. Structural anisotropy results in strain-tunable electronic and optical properties in monolayer  $\text{GeX}$  and  $\text{SnX}$  ( $X = \text{S}, \text{Se}, \text{Te}$ ). *J. Chem. Phys.* **144**, 114708 (2016).
- Rabe, K. M., Ahn, C. H. & Triscone, J.-M. *Physics of Ferroelectrics: A Modern Perspective*. Vol. 105 (Springer Science & Business Media, 2007).
- Setter, N. et al. Ferroelectric thin films: review of materials, properties, and applications. *J. Appl. Phys.* **100**, 051606 (2006).

54. Lee, H. J. et al. Controllable piezoelectricity of Pb (Zr<sub>0.2</sub>Ti<sub>0.8</sub>)O<sub>3</sub> film via in situ misfit strain. *Appl. Phys. Lett.* **110**, 032901 (2017).
55. Tanaka, Y. et al. Strain-driven control of piezoelectricity in (Na, Bi)TiO<sub>3</sub>-BaTiO<sub>3</sub> epitaxial thin films. *Appl. Phys. Lett.* **102**, 192901 (2013).
56. Lee, J. H. et al. A strong ferroelectric ferromagnet created by means of spin-lattice coupling. *Nature* **466**, 954–958 (2010).
57. Hill, N. A. Why are there so few magnetic ferroelectrics? *J. Phys. Chem. B* **104**, 6694–6709 (2000).
58. Spaldin, N. A., Cheong, S.-W. & Ramesh, R. Multiferroics: past, present, and future. *Phys. Today* **63**, 38–43 (2010).
59. Schlom, D. G., Chen, L. Q., Pan, X., Schmehl, A. & Zurbuchen, M. A. A thin film approach to engineering functionality into oxides. *J. Am. Ceram. Soc.* **91**, 2429–2454 (2008).
60. Rondinelli, J. M. & Spaldin, N. A. Structure and properties of functional oxide thin films: insights from electronic-structure calculations. *Adv. Mater.* **23**, 3363–3381 (2011).
61. Uecker, R. et al. Spiral formation during Czochralski growth of rare-earth scandates. *J. Cryst. Growth* **295**, 84–91 (2006).
62. Martin, L. W. & Schlom, D. G. Advanced synthesis techniques and routes to new single-phase multiferroics. *Curr. Opin. Solid State Mater. Sci.* **16**, 199–215 (2012).
63. Tsukada, A., Yamamoto, H. & Naito, M. Doping of Ce in T-La<sub>2</sub>CuO<sub>4</sub>: rigorous test for electron-hole symmetry for high-T<sub>c</sub> superconductivity. *Phys. Rev. B* **74**, 174515 (2006).
64. Schlom, D. G. et al. Elastic strain engineering of ferroic oxides. *Mrs Bull.* **39**, 118–130 (2014).
65. Tokura, Y., Seki, S. & Nagaosa, N. Multiferroics of spin origin. *Rep. Prog. Phys.* **77**, 076501 (2014).
66. Fiebig, M., Lottermoser, T., Meier, D. & Trassin, M. The evolution of multiferroics. *Nat. Rev. Mater.* **1**, 16046 (2016).
67. Kenzelmann, M. et al. Direct transition from a disordered to a multiferroic phase on a triangular lattice. *Phys. Rev. Lett.* **98**, 267205 (2007).
68. Park, S., Choi, Y. J., Zhang, C. L. & Cheong, S. W. Ferroelectricity in an S=1/2 chain cuprate. *Phys. Rev. Lett.* **98**, 057601 (2007).
69. Petrosyan, A. G. et al. Bridgman growth and characterization of LuAlO<sub>3</sub>-Ce<sup>3+</sup> scintillator crystals. *Cryst. Res. Technol.* **33**, 241–248 (1998).
70. Asano, H., Kubo, S., Michikami, O., Satoh, M. & Konaka, T. Epitaxial growth of EuBa<sub>2</sub>Cu<sub>3</sub>O<sub>7-y</sub> films on YAlO<sub>3</sub> single crystals. *Jpn. J. Appl. Phys.* **29**, L1452 (1990).
71. Brown, R., Pendrick, V., Kalokitis, D. & Chai, B. Low-loss substrate for microwave application of high-temperature superconductor films. *Appl. Phys. Lett.* **57**, 1351–1353 (1990).
72. Berkstresser, G. W., Valentino, A. J. & Brandle, C. D. Growth of single crystals of lanthanum aluminate. *J. Cryst. Growth* **109**, 467–471 (1991).
73. Hontsu, S., Ishii, J., Kawai, T. & Kawai, S. LaSrGaO<sub>4</sub> substrate gives oriented crystalline YBa<sub>2</sub>Cu<sub>3</sub>O<sub>7-y</sub> films. *Appl. Phys. Lett.* **59**, 2886–2888 (1991).
74. Rabe, K. M., Dawber, M., Lichtensteiger, C., Ahn, C. H. & Triscone, J.-M. In *Modern Physics of Ferroelectrics: Essential Background 1–30* (Springer, 2007).
75. Berkstresser, G. W., Valentino, A. J. & Brandle, C. D. Growth of single crystals of rare earth gallates. *J. Cryst. Growth* **109**, 457–466 (1991).
76. Sandstrom, R. L. et al. Lanthanum gallate substrates for epitaxial high-temperature superconducting thin films. *Appl. Phys. Lett.* **53**, 1874–1876 (1988).
77. Coh, S. et al. Si-compatible candidates for high-κ dielectrics with the Pbnm perovskite structure. *Phys. Rev. B* **82**, 064101 (2010).
78. Ito, K., Tezuka, K. & Hinatsu, Y. Preparation, magnetic susceptibility, and specific heat on interlanthanide perovskites ABO<sub>3</sub> (A = La–Nd, B = Dy–Lu). *J. Solid State Chem.* **157**, 173–179 (2001).
79. Ovanesyan, K. L., Petrosyan, A. G., Shirinyan, G. O., Pedrini, C. & Zhang, L. Czochralski single crystal growth of Ce- and Pr-doped LaLuO<sub>3</sub> double oxide. *J. Cryst. Growth* **198**, 497–500 (1999).
80. Resta, R. Macroscopic polarization in crystalline dielectrics: the geometric phase approach. *Rev. Mod. Phys.* **66**, 899 (1994).
81. King-Smith, R. & Vanderbilt, D. Theory of polarization of crystalline solids. *Phys. Rev. B* **47**, 1651 (1993).
82. Jo, J. Y. et al. Piezoelectricity in the dielectric component of nanoscale dielectric-ferroelectric superlattices. *Phys. Rev. Lett.* **104**, 207601 (2010).
83. Kunc, K. & Resta, R. External fields in the self-consistent theory of electronic states: a new method for direct evaluation of macroscopic and microscopic dielectric response. *Phys. Rev. Lett.* **51**, 686 (1983).
84. Umari, P. & Pasquarello, A. Ab initio molecular dynamics in a finite homogeneous electric field. *Phys. Rev. Lett.* **89**, 157602 (2002).
85. Sai, N., Rabe, K. M. & Vanderbilt, D. Theory of structural response to macroscopic electric fields in ferroelectric systems. *Phys. Rev. B* **66**, 104108 (2002).
86. Souza, I., Íñiguez, J. & Vanderbilt, D. First-principles approach to insulators in finite electric fields. *Phys. Rev. Lett.* **89**, 117602 (2002).
87. Nenciu, G. Dynamics of band electrons in electric and magnetic fields: rigorous justification of the effective Hamiltonians. *Rev. Mod. Phys.* **63**, 91 (1991).
88. Kane, E. O. Zener tunneling in semiconductors. *J. Phys. Chem. Solids* **12**, 181–188 (1960).
89. Stengel, M. & Vanderbilt, D. Berry-phase theory of polar discontinuities at oxide-oxide interfaces. *Phys. Rev. B* **80**, 241103 (2009).
90. Hong, J. & Vanderbilt, D. Mapping the energy surface of PbTiO<sub>3</sub> in multi-dimensional electric-displacement space. *Phys. Rev. B* **84**, 115107 (2011).
91. Roy, A., Stengel, M. & Vanderbilt, D. First-principles study of high-field piezoelectricity in tetragonal PbTiO<sub>3</sub>. *Phys. Rev. B* **81**, 014102 (2010).
92. Stengel, M., Fennie, C. J. & Ghosez, P. Electrical properties of improper ferroelectrics from first principles. *Phys. Rev. B* **86**, 094112 (2012).
93. Diéguez, O. & Vanderbilt, D. First-principles calculations for insulators at constant polarization. *Phys. Rev. Lett.* **96**, 056401 (2006).
94. Stengel, M., Vanderbilt, D. & Spaldin, N. A. First-principles modeling of ferroelectric capacitors via constrained displacement field calculations. *Phys. Rev. B* **80**, 224110 (2009).
95. Hong, J. & Vanderbilt, D. Electrically driven octahedral rotations in SrTiO<sub>3</sub> and PbTiO<sub>3</sub>. *Phys. Rev. B* **87**, 064104 (2013).
96. Wu, Z. & Cohen, R. E. Pressure-induced anomalous phase transitions and colossal enhancement of piezoelectricity in PbTiO<sub>3</sub>. *Phys. Rev. Lett.* **95**, 037601 (2005).
97. Ahart, M. et al. Origin of morphotropic phase boundaries in ferroelectrics. *Nature* **451**, 545 (2008).
98. Prodan, E. & Kohn, W. Nearsightedness of electronic matter. *Proc. Natl Acad. Sci. USA* **102**, 11635–11638 (2005).
99. Swartz, C. W. & Wu, X. Modeling functional piezoelectricity in perovskite superlattices with competing instabilities. *Phys. Rev. B* **85**, 054102 (2012).
100. Marzari, N., Mostofi, A. A., Yates, J. R., Souza, I. & Vanderbilt, D. Maximally localized Wannier functions: theory and applications. *Rev. Mod. Phys.* **84**, 1419 (2012).
101. Wu, X., Diéguez, O., Rabe, K. M. & Vanderbilt, D. Wannier-based definition of layer polarizations in perovskite superlattices. *Phys. Rev. Lett.* **97**, 107602 (2006).
102. Wu, X., Rabe, K. M. & Vanderbilt, D. Interfacial enhancement of ferroelectricity in CaTiO<sub>3</sub>/BaTiO<sub>3</sub> superlattices. *Phys. Rev. B* **83**, 020104 (2011).
103. Ghosez, P., Gonze, X. & Michenaud, J.-P. Lattice dynamics and ferroelectric instability of barium titanate. *Ferroelectrics* **194**, 39–54 (1997).
104. Ghosez, P., Cockayne, E., Waghmare, U. V. & Rabe, K. M. Lattice dynamics of BaTiO<sub>3</sub>, PbTiO<sub>3</sub>, and PbZrO<sub>3</sub>: a comparative first-principles study. *Phys. Rev. B* **60**, 836 (1999).
105. Cochran, W. Crystal stability and the theory of ferroelectricity. *Adv. Phys.* **9**, 387–423 (1960).
106. Lines, M. E. & Glass, A. M. *Principles and applications of ferroelectrics and related materials*. (Oxford University Press, 2001).
107. Ghosez, P., Gonze, X. & Michenaud, J.-P. Coulomb interaction and ferroelectric instability of BaTiO<sub>3</sub>. *Europhys. Lett.* **33**, 713 (1996).
108. Samara, G. A., Sakudo, T. & Yoshimitsu, K. Important generalization concerning the role of competing forces in displacive phase transitions. *Phys. Rev. Lett.* **35**, 1767 (1975).
109. Choi, K. J. et al. Enhancement of ferroelectricity in strained BaTiO<sub>3</sub> thin films. *Science* **306**, 1005–1009 (2004).
110. Zhang, Y., Liu, M., Wang, J., Shimada, T. & Kitamura, T. Strain tunable ferroelectric and dielectric properties of BaZrO<sub>3</sub>. *J. Appl. Phys.* **115**, 224107 (2014).
111. Diéguez, O., Rabe, K. M. & Vanderbilt, D. First-principles study of epitaxial strain in perovskites. *Phys. Rev. B* **72**, 144101 (2005).
112. Diéguez, O. & Vanderbilt, D. First-principles modeling of strain in perovskite ferroelectric thin films. *Phase Transit.* **81**, 607–622 (2008).
113. Pertsev, N. A., Zembilgotov, A. G. & Tagantsev, A. K. Effect of mechanical boundary conditions on phase diagrams of epitaxial ferroelectric thin films. *Phys. Rev. Lett.* **80**, 1988 (1998).
114. Sai, N. & Vanderbilt, D. First-principles study of ferroelectric and antiferrodistortive instabilities in tetragonal SrTiO<sub>3</sub>. *Phys. Rev. B* **62**, 13942 (2000).
115. Eklund, C.-J., Fennie, C. J. & Rabe, K. M. Strain-induced ferroelectricity in orthorhombic CaTiO<sub>3</sub> from first principles. *Phys. Rev. B* **79**, 220101 (2009).
116. Bhattacharjee, S., Bousquet, E. & Ghosez, P. Engineering multiferroism in CaMnO<sub>3</sub>. *Phys. Rev. Lett.* **102**, 117602 (2009).
117. Wang, H., He, L. & Wu, X. Room temperature multiferroism in CaTcO<sub>3</sub> by interface engineering. *Comput. Mater. Sci.* **96**, 171–177 (2015).
118. Vanderbilt, D. & Zhong, W. First-principles theory of structural phase transitions for perovskites: competing instabilities. *Ferroelectrics* **206**, 181–204 (1998).
119. Ali, R. & Yashima, M. Space group and crystal structure of the perovskite CaTiO<sub>3</sub> from 296 to 1720 K. *J. Solid State Chem.* **178**, 2867–2872 (2005).
120. Zalar, B. et al. NMR study of disorder in BaTiO<sub>3</sub> and SrTiO<sub>3</sub>. *Phys. Rev. B* **71**, 064107 (2005).
121. Kvyatkovskii, O. E. Quantum effects in incipient and low-temperature ferroelectrics (a review). *Phys. Solid State* **43**, 1401–1419 (2001).

122. Zhong, W. & Vanderbilt, D. Effect of quantum fluctuations on structural phase transitions in SrTiO<sub>3</sub> and BaTiO<sub>3</sub>. *Phys. Rev. B* **53**, 5047 (1996).
123. Zhong, W. & Vanderbilt, D. Competing structural instabilities in cubic perovskites. *Phys. Rev. Lett.* **74**, 2587 (1995).
124. Pertsev, N., Tagantsev, A. & Setter, N. Phase transitions and strain-induced ferroelectricity in SrTiO<sub>3</sub> epitaxial thin films. *Phys. Rev. B* **61**, R825 (2000).
125. Barrett, J. H. Dielectric constant in perovskite type crystals. *Phys. Rev.* **86**, 118 (1952).
126. Antons, A., Neaton, J., Rabe, K. M. & Vanderbilt, D. Tunability of the dielectric response of epitaxially strained SrTiO<sub>3</sub> from first principles. *Phys. Rev. B* **71**, 024102 (2005).
127. Yamada, T. et al. In-plane and out-of-plane ferroelectric instabilities in epitaxial SrTiO<sub>3</sub> films. *Phys. Rev. Lett.* **96**, 157602 (2006).
128. Gu, Y., Rabe, K., Bousquet, E., Gopalan, V. & Chen, L.-Q. Phenomenological thermodynamic potential for CaTiO<sub>3</sub> single crystals. *Phys. Rev. B* **85**, 064117 (2012).
129. Cockayne, E. & Burton, B. P. Phonons and static dielectric constant in CaTiO<sub>3</sub> from first principles. *Phys. Rev. B* **62**, 3735 (2000).
130. Akamatsu, H. et al. Strong spin-lattice coupling through oxygen octahedral rotation in divalent europium perovskites. *Adv. Funct. Mater.* **23**, 1864–1872 (2013).
131. Birol, T. & Fennie, C. J. Origin of giant spin-lattice coupling and the suppression of ferroelectricity in EuTiO<sub>3</sub> from first principles. *Phys. Rev. B* **88**, 094103 (2013).
132. Akamatsu, H. et al. Antiferromagnetic superexchange via 3d states of titanium in EuTiO<sub>3</sub> as seen from hybrid Hartree-Fock density functional calculations. *Phys. Rev. B* **83**, 214421 (2011).
133. Garcia-Fernandez, P., Aramburu, J. A. & Moreno, M. Influence of magnetic ordering on structural instabilities in insulating perovskites. *Phys. Rev. B* **83**, 174406 (2011).
134. Hong, J., Stroppa, A., Íñiguez, J., Picozzi, S. & Vanderbilt, D. Spin-phonon coupling effects in transition-metal perovskites: A DFT+U and hybrid-functional study. *Phys. Rev. B* **85**, 054417 (2012).
135. Brous, J., Fankuchen, I. & Banks, E. Rare earth titanates with a perovskite structure. *Acta Crystallogr.* **6**, 67–70 (1953).
136. Yang, Y., Ren, W., Wang, D. & Bellaiche, L. Understanding and revisiting properties of EuTiO<sub>3</sub> bulk material and films from first principles. *Phys. Rev. Lett.* **109**, 267602 (2012).
137. Katsufuji, T. & Takagi, H. Coupling between magnetism and dielectric properties in quantum paraelectric EuTiO<sub>3</sub>. *Phys. Rev. B* **64**, 054415 (2001).
138. Chien, C.-L., DeBenedetti, S. & Barros, F. D. S. Magnetic properties of EuTiO<sub>3</sub>, Eu<sub>2</sub>TiO<sub>4</sub>, and Eu<sub>3</sub>Ti<sub>2</sub>O<sub>7</sub>. *Phys. Rev. B* **10**, 3913 (1974).
139. Goodenough, J. B. Theory of the role of covalence in the perovskite-type manganites [La,M(II)]MnO<sub>3</sub>. *Phys. Rev.* **100**, 564 (1955).
140. Kanamori, J. Superexchange interaction and symmetry properties of electron orbitals. *J. Phys. Chem. Solids* **10**, 87–98 (1959).
141. Yamauchi, K. & Picozzi, S. Magnetically induced ferroelectricity in TbMnO<sub>3</sub>: inverse Goodenough–Kanamori interaction. *J. Phys.* **21**, 064203 (2009).
142. Imada, M., Fujimori, A. & Tokura, Y. Metal-insulator transitions. *Rev. Mod. Phys.* **70**, 1039 (1998).
143. Yang, Z., Ko, C. & Ramanathan, S. Oxide electronics utilizing ultrafast metal-insulator transitions. *Annu. Rev. Mater. Res.* **41**, 337–367 (2011).
144. Kugel', K. I. & Khomskii, D. I. The Jahn-Teller effect and magnetism: transition metal compounds. *Sov. Phys. Uspekhi* **25**, 231–256 (1982).
145. Burns, R. G. *Mineralogical Applications of Crystal Field Theory*. Vol. 5 (Cambridge University Press, 1993).
146. Goodenough, J. B. Jahn-Teller phenomena in solids. *Annu. Rev. Mater. Sci.* **28**, 1–27 (1998).
147. Birol, T. et al. The magnetoelectric effect in transition metal oxides: insights and the rational design of new materials from first principles. *Curr. Opin. Solid State Mater. Sci.* **16**, 227–242 (2012).
148. Song, G. & Zhang, W. First-principles study on the phase diagram and multi-ferroic properties of (SrCoO<sub>3</sub>)<sub>1-x</sub>(SrTiO<sub>3</sub>)<sub>x</sub> superlattices. *Sci. Rep.* **4**, 4564 (2014).
149. Lee, J. H. et al. Strongly coupled magnetic and electronic transitions in multivalent strontium cobaltites. *Sci. Rep.* **7**, 16066 (2017).
150. Xiang, H., Lee, C., Koo, H.-J., Gong, X. & Whangbo, M.-H. Magnetic properties and energy-mapping analysis. *Dalton Trans.* **42**, 823–853 (2013).
151. Varignon, J., Bristowe, N. C. & Ghosez, P. Electric field control of Jahn-Teller distortions in bulk perovskites. *Phys. Rev. Lett.* **116**, 057602 (2016).
152. Bhattacharya, A. & May, S. J. Magnetic oxide heterostructures. *Annu. Rev. Mater. Res.* **44**, 65–90 (2014).
153. Bibes, M., Villegas, J. E. & Barthelemy, A. Ultrathin oxide films and interfaces for electronics and spintronics. *Adv. Phys.* **60**, 5–84 (2011).
154. Zubko, P., Gariglio, S., Gabay, M., Ghosez, P. & Triscone, J.-M. Interface physics in complex oxide heterostructures. *Annu. Rev. Condens. Matter Phys.* **2**, 141–165 (2011).
155. Hwang, H. Y. et al. Emergent phenomena at oxide interfaces. *Nat. Mater.* **11**, 103–113 (2012).
156. Ahn, C. H., Rabe, K. M. & Triscone, J.-M. Ferroelectricity at the nanoscale: local polarization in oxide thin films and heterostructures. *Science* **303**, 488–491 (2004).
157. Sai, N., Meyer, B. & Vanderbilt, D. Ferroelectric and piezoelectric properties in the presence of compositionally broken inversion symmetry. *AIP Conf. Proc.* **582**, 218–227 (2001).
158. Yamada, H., Kawasaki, M., Ogawa, Y. & Tokura, Y. Perovskite oxide tricolor superlattices with artificially broken inversion symmetry by interface effects. *Appl. Phys. Lett.* **81**, 4793–4795 (2002).
159. Shen, J. & Ma, Y.-q. Long-range coupling interactions in ferroelectric superlattices. *Phys. Rev. B* **61**, 14279 (2000).
160. Perez-Mato, J. et al. Competing structural instabilities in the ferroelectric Aurivillius compound SrBi<sub>2</sub>Ta<sub>2</sub>O<sub>9</sub>. *Phys. Rev. B* **70**, 214111 (2004).
161. Hatch, D. M. & Stokes, H. T. Complete listing of order parameters for a crystalline phase transition: a solution to the generalized inverse Landau problem. *Phys. Rev. B* **65**, 014113 (2001).
162. Bousquet, E. et al. Improper ferroelectricity in perovskite oxide artificial superlattices. *Nature* **452**, 732–736 (2008).
163. Perez-Mato, J. M., Orobengoa, D. & Aroyo, M. I. Mode crystallography of distorted structures. *Acta Crystallogr. Sect. A* **66**, 558–590 (2010).
164. May, S. J. et al. Quantifying octahedral rotations in strained perovskite oxide films. *Phys. Rev. B* **82**, 014110 (2010).
165. Thomas, N. W. The compositional dependence of octahedral tilting in orthorhombic and tetragonal perovskites. *Acta Crystallogr. Sect. B* **52**, 16–31 (1996).
166. Angel, R. J., Zhao, J. & Ross, N. L. General rules for predicting phase transitions in perovskites due to octahedral tilting. *Phys. Rev. Lett.* **95**, 025503 (2005).
167. Thomas, N. W. & Beitollahi, A. Inter-relationship of octahedral geometry, polyhedral volume ratio and ferroelectric properties in rhombohedral perovskites. *Acta Crystallogr. Sect. B* **50**, 549–560 (1994).
168. Bilc, D. I. & Singh, D. J. Frustration of tilts and A-site driven ferroelectricity in KNbO<sub>3</sub>-LiNbO<sub>3</sub> Alloys. *Phys. Rev. Lett.* **96**, 147602 (2006).
169. Woodward, P. M. Octahedral tilting in perovskites. II. Structure stabilizing forces. *Acta Crystallogr. Sect. B* **53**, 44–66 (1997).
170. Benedek, N. A. & Fennie, C. J. Hybrid improper ferroelectricity: a mechanism for controllable polarization-magnetization coupling. *Phys. Rev. Lett.* **106**, 107204 (2011).
171. Kida, N. et al. Optical magnetoelectric effect of patterned oxide superlattices with ferromagnetic interfaces. *Phys. Rev. Lett.* **99**, 197404 (2007).
172. Takahashi, Y., Shimano, R., Kaneko, Y., Murakawa, H. & Tokura, Y. Magneto-electric resonance with electromagnons in a perovskite helimagnet. *Nat. Phys.* **8**, 121 (2012).
173. Barron, L. D. & Urbancich, J. Magneto-chiral birefringence and dichroism. *Mol. Phys.* **51**, 715–730 (1984).
174. Urtiev, F. A., Kukhar, V. G. & Pertsev, N. A. Phase diagrams of single-domain ferroelectric-dielectric superlattices. *Appl. Phys. Lett.* **90**, 252910 (2007).
175. Johnston, K., Huang, X., Neaton, J. B. & Rabe, K. M. First-principles study of symmetry lowering and polarization in BaTiO<sub>3</sub>/SrTiO<sub>3</sub> superlattices with in-plane expansion. *Phys. Rev. B* **71**, 100103 (2005).
176. Nakhmanson, S. M., Rabe, K. & Vanderbilt, D. Polarization enhancement in two- and three-component ferroelectric superlattices. *Appl. Phys. Lett.* **87**, 102906 (2005).
177. Kim, L., Kim, J., Waghmare, U. V., Jung, D. & Lee, J. Structural transition and dielectric response of an epitaxially strained BaTiO<sub>3</sub>/SrTiO<sub>3</sub> superlattice: a first-principles study. *Phys. Rev. B* **72**, 214121 (2005).
178. Kim, L., Kim, J., Jung, D., Lee, J. & Waghmare, U. V. Polarization of strained BaTiO<sub>3</sub>/SrTiO<sub>3</sub> artificial superlattice: First-principles study. *Appl. Phys. Lett.* **87**, 052903 (2005).
179. Tian, W. et al. Structural evidence for enhanced polarization in a commensurate short-period BaTiO<sub>3</sub>/SrTiO<sub>3</sub> superlattice. *Appl. Phys. Lett.* **89**, 092905 (2006).
180. Li, Y. L. et al. Prediction of ferroelectricity in BaTiO<sub>3</sub>/SrTiO<sub>3</sub> superlattices with domains. *Appl. Phys. Lett.* **91**, 112914 (2007).
181. Li, Y. L. et al. Interfacial coherency and ferroelectricity of BaTiO<sub>3</sub>/SrTiO<sub>3</sub> superlattice films. *Appl. Phys. Lett.* **91**, 252904 (2007).
182. Lisenkov, S. & Bellaiche, L. Phase diagrams of BaTiO<sub>3</sub>/SrTiO<sub>3</sub> superlattices from first principles. *Phys. Rev. B* **76**, 020102 (2007).
183. Christen, H. M. et al. The growth and properties of epitaxial KNbO<sub>3</sub> thin films and KNbO<sub>3</sub>/KTAO<sub>3</sub> superlattices. *Appl. Phys. Lett.* **68**, 1488–1490 (1996).
184. Christen, H.-M., Specht, E. D., Norton, D. P., Chisholm, M. F. & Boatner, L. A. Long-range ferroelectric interactions in KTAO<sub>3</sub>/KNbO<sub>3</sub> superlattice structures. *Appl. Phys. Lett.* **72**, 2535–2537 (1998).
185. Sepiarsky, M., Phillpot, S. R., Wolf, D., Stachiotti, M. G. & Migoni, R. L. Long-ranged ferroelectric interactions in perovskite superlattices. *Phys. Rev. B* **64**, 060101 (2001).

186. Hao, S. et al. Spontaneous polarizations of ultrashort-period epitaxial  $\text{KNbO}_3/(\text{KTaO}_3)_m$  superlattices: an ab initio investigation. *Appl. Phys. Lett.* **86**, 232903 (2005).
187. Cooper, V. R., Johnston, K. & Rabe, K. M. Polarization enhancement in short period superlattices via interfacial intermixing. *Phys. Rev. B* **76**, 020103 (2007).
188. Samara, G. A. & Morosin, B. Anharmonic effects in  $\text{KTaO}_3$ : ferroelectric mode, thermal expansion, and compressibility. *Phys. Rev. B* **8**, 1256 (1973).
189. Hewat, A. W. Soft modes and the structure, spontaneous polarization and Curie constants of perovskite ferroelectrics: tetragonal potassium niobate. *J. Phys. C* **6**, 1074 (1973).
190. Dawber, M. et al. Tailoring the properties of artificially layered ferroelectric superlattices. *Adv. Mater.* **19**, 4153–4159 (2007).
191. Sinsheimer, J. et al. Engineering polarization rotation in a ferroelectric superlattice. *Phys. Rev. Lett.* **109**, 167601 (2012).
192. Kornev, I. A., Bellaiche, L., Janolin, P.-E., Khlil, B. & Suard, E. Phase diagram of  $\text{Pb}(\text{Zr,Ti})\text{O}_3$  solid solutions from first principles. *Phys. Rev. Lett.* **97**, 157601 (2006).
193. Cohen, R. E. Origin of ferroelectricity in perovskite oxides. *Nature* **358**, 136–138 (1992).
194. Cohen, R. E. & Krakauer, H. Electronic structure studies of the differences in ferroelectric behavior of  $\text{BaTiO}_3$  and  $\text{PbTiO}_3$ . *Ferroelectrics* **136**, 65–83 (1992).
195. Perez-Mato, J. et al. Multiple instabilities in  $\text{Bi}_4\text{Ti}_3\text{O}_{12}$ : a ferroelectric beyond the soft-mode paradigm. *Phys. Rev. B* **77**, 184104 (2008).
196. Fennie, C. J. & Rabe, K. M. Ferroelectric transition in  $\text{YMnO}_3$  from first principles. *Phys. Rev. B* **72**, 100103 (2005).
197. Fiebig, M. Revival of the magnetoelectric effect. *J. Phys. D* **38**, R123 (2005).
198. Nowadnick, E. A. & Fennie, C. J. Domains and ferroelectric switching pathways in  $\text{Ca}_3\text{Ti}_2\text{O}_7$  from first principles. *Phys. Rev. B* **94**, 104105 (2016).
199. Stroppa, A., Barone, P., Jain, P., Perez-Mato, J. M. & Picozzi, S. Hybrid improper ferroelectricity in a multiferroic and magnetoelectric metal-organic framework. *Adv. Mater.* **25**, 2284–2290 (2013).
200. Benedek, N. A., Mulder, A. T. & Fennie, C. J. Polar octahedral rotations: a path to new multifunctional materials. *J. Solid State Chem.* **195**, 11–20 (2012).
201. Blok, J. L., Blank, D. H., Rijnders, G., Rabe, K. M. & Vanderbilt, D. Interplay of epitaxial strain and rotations in  $\text{PbTiO}_3/\text{PbZrO}_3$  superlattices from first principles. *Phys. Rev. B* **84**, 205413 (2011).
202. Glazer, A. M. The classification of tilted octahedra in perovskites. *Acta Crystallogr. Sect. B* **28**, 3384–3392 (1972).
203. Sim, H., Cheong, S. & Kim, B. G. Octahedral tilting-induced ferroelectricity in  $\text{ASnO}_3/\text{A}'\text{SnO}_3$  superlattices (A, A' = Ca, Sr, and Ba). *Phys. Rev. B* **88**, 014101 (2013).
204. Ghosh, S., Das, H. & Fennie, C. J. Linear magnetoelectricity at room temperature in perovskite superlattices by design. *Phys. Rev. B* **92**, 184112 (2015).
205. Zanolli, Z., Wojdeł, J. C., Iñiguez, J. & Ghosez, P. Electric control of the magnetization in  $\text{BiFeO}_3/\text{LaFeO}_3$  superlattices. *Phys. Rev. B* **88**, 060102 (2013).
206. Dzyaloshinsky, I. A thermodynamic theory of “weak” ferromagnetism of antiferromagnetics. *J. Phys. Chem. Solids* **4**, 241–255 (1958).
207. Moriya, T. Anisotropic superexchange interaction and weak ferromagnetism. *Phys. Rev.* **120**, 91 (1960).
208. Das, H., Waghmare, U. V., Saha-Dasgupta, T. & Sarma, D. D. Electronic structure, phonons, and dielectric anomaly in ferromagnetic insulating double perovskite  $\text{La}_2\text{NiMnO}_6$ . *Phys. Rev. Lett.* **100**, 186402 (2008).
209. Das, H., Waghmare, U. V., Saha-Dasgupta, T. & Sarma, D. D. Theoretical evidence and chemical origin of the magnetism-dependent electrostructural coupling in  $\text{La}_2\text{NiMnO}_6$ . *Phys. Rev. B* **79**, 144403 (2009).
210. Zhao, H. J. et al. Near room-temperature multiferroic materials with tunable ferromagnetic and electrical properties. *Nat. Commun.* **5**, 4021 (2014).
211. Howard, C. J. & Stokes, H. T. Group-theoretical analysis of octahedral tilting in perovskites. *Acta Crystallogr. Sect. B* **54**, 782–789 (1998).
212. Wang, J. et al. Epitaxial  $\text{BiFeO}_3$  multiferroic thin film heterostructures. *Science* **299**, 1719–1722 (2003).
213. Barker, A. S. & Loudon, R. Dielectric properties and optical phonons in  $\text{LiNbO}_3$ . *Phys. Rev.* **158**, 433 (1967).
214. Kuo, C. Y. et al. Single-domain multiferroic  $\text{BiFeO}_3$  films. *Nat. Commun.* **7**, 12712 (2016).
215. Zhou, Q. *First-Principles Modeling of Functional Perovskite Materials and Superlattices*. (Rutgers University-Graduate School, New Brunswick, 2014).
216. Goldschmidt, V. M. Die Gesetze der Kristallochemie. *Naturwissenschaften* **14**, 477–485 (1926).
217. Lufaso, M. W. & Woodward, P. M. Prediction of the crystal structures of perovskites using the software program SPuDS. *Acta Crystallogr. Sect. B* **57**, 725–738 (2001).
218. Wang, H., He, L. & Wu, X. Interface enhancement of spin-polar phonon coupling in perovskite multiferroic superlattices. *Europhys. Lett.* **100**, 17005 (2012).
219. Seo, S. S. A. et al. Ferroelectricity in artificial bicolor oxide superlattices. *Adv. Mater.* **19**, 2460–2464 (2007).
220. Seo, S. S. A. & Lee, H. N. Strain-coupled ferroelectric polarization in  $\text{BaTiO}_3\text{-CaTiO}_3$  superlattices. *Appl. Phys. Lett.* **94**, 232904 (2009).
221. Jo, J. Y. et al. Component-specific electromechanical response in a ferroelectric/dielectric superlattice. *Phys. Rev. B* **82**, 174116 (2010).
222. Shen, H., Xu, J., Wu, A., Zhao, J. & Shi, M. Magnetic and thermal properties of perovskite  $\text{YFeO}_3$  single crystals. *Mater. Sci. Eng.* **157**, 77–80 (2009).
223. Fu, X., Xi, X., Bi, K. & Zhou, J. Temperature-dependent terahertz magnetic dipole radiation from antiferromagnetic  $\text{GdFeO}_3$  ceramics. *Appl. Phys. Lett.* **103**, 211108 (2013).
224. Zhu, W., Pi, L., Tan, S. & Zhang, Y. Anisotropy and extremely high coercivity in weak ferromagnetic  $\text{LuFeO}_3$ . *Appl. Phys. Lett.* **100**, 052407 (2012).
225. Mundy, J. A. et al. Atomically engineered ferroic layers yield a room-temperature magnetoelectric multiferroic. *Nature* **537**, 523–527 (2016).

## ACKNOWLEDGEMENTS

This work was supported by National Science Foundation through Awards No. DMR-1552287.

## AUTHOR CONTRIBUTIONS

X.W. designed the project; all authors contributed to the writing of the paper.

## COMPETING INTERESTS

The authors declare no competing interests.

## ADDITIONAL INFORMATION

**Correspondence** and requests for materials should be addressed to X.W.

**Reprints and permission information** is available at <http://www.nature.com/reprints>

**Publisher's note** Springer Nature remains neutral with regard to jurisdictional claims in published maps and institutional affiliations.



**Open Access** This article is licensed under a Creative Commons Attribution 4.0 International License, which permits use, sharing, adaptation, distribution and reproduction in any medium or format, as long as you give appropriate credit to the original author(s) and the source, provide a link to the Creative Commons license, and indicate if changes were made. The images or other third party material in this article are included in the article's Creative Commons license, unless indicated otherwise in a credit line to the material. If material is not included in the article's Creative Commons license and your intended use is not permitted by statutory regulation or exceeds the permitted use, you will need to obtain permission directly from the copyright holder. To view a copy of this license, visit <http://creativecommons.org/licenses/by/4.0/>.

© The Author(s) 2020